Supplementary Information for

High entropy sulfonium-based organic ionic plastic crystals for sustainable cooling

Samantha L. Piper, Amy L. Thomson, Durga Acharya, Cara M. Doherty, Luke A. O'Dell, Douglas R. MacFarlane and Jennifer M. Pringle

E-mails: jenny.pringle@deakin.edu.au, douglas.macfarlane@monash.edu

Table S1. Thermal properties of the solid-solid (s-s) and melting (m) transitions of the BC OIPCs, determined by differential scanning calorimetry using a scan rate of 10 °C min^{-1}.

OIPC	M_w / g mol^{-1}	$T_{s\text{-}s}$ / °C	$\Delta H_{s\text{-}s}$ / J g^{-1}	$\Delta H_{s\text{-}s}$ / kJ mol^{-1}	$\Delta S_{s\text{-}s}$ / J kg^{-1} K^{-1}	$\Delta S_{s\text{-}s}$ / J mol^{-1} K^{-1}	T_m / °C	ΔH_m / J g^{-1}	ΔH_m / kJ mol^{-1}	ΔS_m / J mol^{-1} K^{-1}
$[S_{111}][FSI]$	257.28	4	82	21	296	76	143	5.6	1.4	5.2
$[S_{112}][FSI]$	271.31	-20	95	26	375	102	101	11	3.1	12
$[S_{(5)1}][FSI]$	283.32	-19	84	24	331	93	184 (decomp)			
$[S_{(5)2}][FSI]$	297.35	-5	92	27	343	102	69	8.4	2.5	9.3
$[N_{1111O1}][FSI]$	284.29	-9	68	19	258	73	78	7.4	2.1	6

1. Materials and methods

1.1 Synthesis of OIPCs

Iodomethane (99%, Acros Organics), iodoethane (99%, Sigma-Aldrich), tetrahydrothiophene (99%, Sigma-Aldrich), sodium bis(fluorosulfonyl)imide (99.9%, Solvionic), acetone (>99.5%, ChemSupply Australia), diethyl ether (>99.7%, RCI Labscan), dichloromethane (>99.5%, RCI Labscan), ethanol (>99.9%, ChemSupply Australia), acetonitrile (>99.9%, RCI Labscan) and deuterium oxide (>99.9%, Sigma-Aldrich) were used as received without further purification.

$[N_{1111O1}][FSI]$ (pictured) was sourced from Boron Molecular (≥97%) and used as received. Purity was confirmed by NMR and DSC analysis. **^{1}H NMR** (400 MHz, D_2O) δ 4.61 (s, 2H), 3.74 (s, 3H), 3.10 (s, 9H). ^{13}C NMR (101 MHz, D_2O) δ 93.5 (t, *J* = 6.4 Hz), 61.2, 49.4 (t, *J* = 7.8 Hz).

$[S_{111}]I$ was sourced from Sigma Aldrich (98%) and was used as received without further purification. Purity was confirmed by NMR analysis. **^{1}H NMR** (400 MHz, D_2O) δ 2.96 (s, 9H). ^{13}C NMR (101 MHz, D_2O) δ 26.8.

Trimethylsulfonium bis(fluorosulfonyl)imide, $[S_{111}][FSI]$

Sodium bis(fluorosulfonyl)imide (5.51 g, 27.1 mmol, 1.05 eq.) was added to a stirring solution of $[S_{111}]I$ (5.26 g, 25.8 mmol, 1 eq.) in water (10 mL). The solution was stirred in darkness at room temperature for 16 hours. The reaction mixture was then transferred to a separating funnel and the product was extracted with dichloromethane (4 x 15 mL). The organic phase was combined and concentrated by rotary evaporation to give $[S_{111}][FSI]$ as a pale white plastic solid (5.35 g, 81%). The solid was purified by recrystallisation in cold (~-25 °C) ethanol to give a white solid. **^{1}H NMR**

(400 MHz, D_2O) δ 2. 94 (s, 9H). m.p.: 143 °C. **^{13}C NMR** (101 MHz, D_2O) δ 26.6. **ES$^-$ HRMS**(*m/z*): $[M]^+$ calcd for $[S_{111}]^+$, 77.04; found, 77.0410. $[M]^-$ calcd for $[FSI]^-$, 179.92; found, 179.9246.

Ethyldimethylsulfonium bis(fluorosulfonyl)imide, [S_{112}][FSI]

Ethyldimethylsulfonium iodide, [S_{112}]I

Dimethylsulfide (5.88 g, 94.6 mmol) and iodoethane (17.17 g, 110 mmol) were combined and stirred under an inert nitrogen atmosphere and in darkness for 10 days, during which time the reaction mixture turned solid. The resulting white crystals were dried under vacuum to remove residual starting materials before being carried through to the next step to avoid decomposition (yield: 21.6 g, 84%). **^{1}H NMR** (400 MHz, D_2O) δ 3.54 (q, 2H, *J* = 7.5 Hz), 3.10 (s, 6H), 1.64 (t, 3H, *J* = 7.5 Hz). **^{13}C NMR** (101 MHz, D_2O) δ 37.7, 24.1, 8.1.

Ethyldimethylsulfonium bis(fluorosulfonyl)imide, [S_{112}][FSI]

[S_{112}]I (4.037 g, 12.5 mmol) was dissolved in water and added to a stirring solution of lithium bis(fluorosulfonyl)imide (4.940 g, 22.7 mmol) in water. The solution was stirred at room temperature in darkness for two hours. The [S_{112}][FSI] product was extracted with dichloromethane (3 x 15 mL). The organic layer was then washed with water (3 x 5 mL) and then concentrated by rotary evaporation to give [S_{112}][FSI] as a colourless plastic solid (pictured). The solid was dried under vacuum at 50 °C for 2 days (yield: 84%). A very small additional peak at 2.93 ppm in the ^{1}H NMR spectra indicates a minor (~1%) impurity of the $[S_{111}]^+$ cation, attributed to the reversibility of the alkylation of sulfides. m.p.: 102 °C **^{1}H NMR** (400 MHz, D_2O) δ 3.43 (q, 2H, J = 7.48 Hz), 2.89 (s, 6H), 1.53 (t, 3H, J = 7.48 Hz). **^{13}C NMR** (101 MHz, D_2O) δ 37.6, 23.6, 7.6. **ES$^-$ HRMS**(*m/z*) : $[M]^+$ calcd for $[S_{112}]^+$, 91.06 ; found, 91.0568. $[M]^-$ calcd for $[FSI]^-$, 179.92; found, 179.9246.

S-methylthiolanium bis(fluorosulfonyl)imide, [$S_{(5)1}$][FSI]

1-methyltetrahydrothiophenium iodide, [$S_{(5)1}$]I

[$S_{(5)1}$]I was first synthesised using a modified version of a known procedure.[1] Iodomethane (10.6 mL, 170 mmol, 3 eq.) was added dropwise to a stirring solution of tetrahydrothiophene (5.00 g, 56.7 mmol, 1 eq.) in acetone (20 mL) under an argon atmosphere. The vessel was shaded from light using aluminium foil. The solution was stirred at room temperature for 2 hours, over which time a large amount of pale yellow precipitate formed. Diethyl ether (50 mL) was added and the solid was collected *via* vacuum filtration and washed with diethyl ether (100 mL), then dried under vacuum to give [$S_{(5)1}$]I as a pale yellow powder (yield: 89%). **^{1}H NMR** (400 MHz, D_2O) δ 3.68 – 3.57 (m, 2H), 3.45 – 3.34 (m, 2H), 2.83 (s, 3H), 2.49 – 2.24 (m, 4H). **^{13}C NMR** (101 MHz, D_2O) δ 44.9, 28.1, 25.2.

S-methylthiolanium bis(fluorosulfonyl)imide, [$S_{(5)1}$][FSI]

[$S_{(5)1}$]I (2.32 g, 101 mmol) was dissolved in water and added to a stirring solution of lithium bis(fluorosulfonyl)imide (1.98 g, 105 mmol) in water. The solution was stirred at room temperature and in darkness for two hours. The [$S_{(5)1}$][FSI] product was extracted with dichloromethane (3 x 15 mL). The organic layer was then washed with water (3 x 5 mL) and then concentrated by rotary evaporation to give [$S_{(5)1}$][FSI] as a pale white plastic solid (pictured). The solid was dried under vacuum at 50 °C for 2 days (yield: 1.94 g, 68%). m.p.:184 °C (decomp). **^{1}H NMR** (400 MHz, D_2O) δ 3.67 – 3.55 (m, 2H), 3.42 – 3.32 (m, 2H), 2.81 (s, 3H), 2.48 – 2.22 (m, 4H). **^{13}C NMR** (101

MHz, D_2O) δ 44.8, 28.0, 25.0. **ES$^-$ HRMS**(*m/z*) : $[M]^+$ calcd for $[S_{(5)1}]^+$, 103.06 ; found, 103.0571. $[M]^-$ calcd for $[FSI]^-$, 179.92; found, 179.9246.

<u>*S*-ethylthiolanium bis(fluorosulfonyl)imide, $[S_{(5)2}][FSI]$</u>

S-ethylthiolanium iodide, $[S_{(5)2}]I$

Iodoethane (17.35 g, 111 mmol) and tetrahydrothiophene (9.34 g, 106 mmol) were combined and stirred under an inert nitrogen atmosphere and in darkness for 10 days, during which time the reaction mixture turned solid. The resulting yellow crystals were dried briefly under vacuum to remove residual liquid starting materials (yield: 58%). **^{1}H NMR** (400 MHz, D_2O) δ 3.64-3.57 (m, 2H), 3.48-3.41 (m, 2H), 3.2585 (q, 2H, J = 7.44 Hz), 2.39-2.30 (m, 4H), 1.46 (t, 3H, J = 7.44 Hz). **^{13}C NMR** (101 MHz, D_2O) δ 42.6, 36.7, 28.3, 9.4.

S-ethylthiolanium bis(fluorosulfonyl)imide, $[S_{(5)2}][FSI]$

$[S_{(5)2}]I$ (1.37 g, 5.6 mmol) was dissolved in water and added to a stirring solution of lithium bis(fluorosulfonyl)imide (1.12 g, 6 mmol) in water. The solution was stirred at room temperature and in darkness for two hours. The $[S_{(5)2}][FSI]$ product was extracted with dichloromethane (3 x 15 mL). The organic layer was then washed with water (3 x 3 mL) and then concentrated by rotary evaporation to give $[S_{(5)2}][FSI]$ as a colourless plastic solid. The solid was dried under vacuum at 50 °C for 2 days (yield: 1.2 g , 72%). m.p.: 69 °C. **^{1}H NMR** (400 MHz, D_2O) δ 3.61-3.38 (m, 4H), 3.22 (q, 2H, J = 7.48), 2.40-2.28 (m, 4H), 1.45 (t, 3H, J = 7.48 Hz). **^{13}C NMR** (101 MHz, D_2O) δ 42.4, 36.6, 28.2, 9.2. **ES$^-$ HRMS**(*m/z*) : $[M]^+$ calcd for $[S_{(5)2}]^+$, 117.07; found, 117.0727. $[M]^-$ calcd for $[FSI]^-$, 179.92; found, 179.9245.

1.2 Differential thermal analysis (DTA) and differential scanning calorimetry (DSC)

Isobaric high-pressure differential thermal analysis (HP-DTA)

High-pressure differential thermal analysis (HP-DTA) data was collected using a bespoke DTA apparatus with silicone oil as the pressure-transmitting medium. The apparatus contains two thermocouples within the pressure cell, to which two glass capillaries can be attached: one containing the sample to be analysed (~100 mg) and the other containing an Al_2O_3 standard reference material. Pressure was applied to the system using a hydraulic pump, and following pressurisation the system was allowed to equilibrate for ~30 minutes prior to the commencement of the experiment. A scanning rate of 1 °C min^{-1} was used, with isothermal holding for one minute at either temperature extreme. Heat flow into and out of the sample was indicated by the temperature difference between the thermocouple immersed within the sample and the thermocouple immersed in the reference, which was plotted as Δ*T* versus the temperature of the thermocouple immersed within the sample. The phase transition temperatures were defined by the onsets of the endo and exothermic peaks unless otherwise specified. The temperature was calibrated by confirming that the 1 bar data was concordant with the DSC data.

Table S2. Transition onset and peak temperatures for $[S_{111}][FSI]$ at various pressures, determined from HP-DTA experiments. Values of ΔT_{hys} correspond to the difference between the onset temperatures of $T_{s\text{-}s}$ and T_c.

Pressure / bar	$T_{s\text{-}s}$ (onset) / °C	$T_{s\text{-}s}$ (peak) / °C	T_c (onset) / °C	T_c (peak) / °C	ΔT_{hys} / °C
1	4.6	5.7	3.4	3.7	1.2
147	6.8	8.0	5.9	5.5	0.9
281	8.7	9.9	7	7.4	1.7
391	10.2	10.6	9.2	7.8	1.0
531	12.2	11.4	11.2	11.1	1.0
668	14.12	15.4	13	13.2	1.2
				Average	1.2

Table S3. Transition onset and peak temperatures for $[S_{112}][FSI]$ at various pressures, determined from HP-DTA experiments. Values of ΔT_{hys} correspond to the difference between the onset temperatures of $T_{s\text{-}s}$ and T_c.

Pressure / bar	$T_{s\text{-}s}$ (onset) / °C	$T_{s\text{-}s}$ (peak) / °C	T_c (onset) / °C	T_c (peak) / °C	ΔT_{hys} / °C
1	-18.3	-17.2	-20.7	-20.2	2.4
225	-15.8	-14.6	-18.8	-18.1	3
420	-13.6	-12.4	-17.5	-17.8	3.9
558	-12.2	-11	-17.4	-17.7	5.2
646	-11.3	-10	-18.5	-18.6	7.2
				Average	4.3

*Per the standard definition, the onset is defined as the intersection between the baseline and the steepest tangent of the peak. Due to the shape of the endothermic peaks, calculated onsets are slightly higher than the temperature at which there is a noticeable deviation from the baseline. Hence, at 1 bar, the $T_{s\text{-}s}$ reported here is slightly (~1 °C) higher than the onset observed in ambient pressure DSC (reported in the manuscript). This is consistent among all heating scans and thus has no effect on the values of $dT_{s\text{-}s}/dp$ ultimately calculated from this data. The reported values of ΔT_{hys} calculated from these onsets are therefore likely slight overestimations.

**As the material self-heats during crystallisation, the standard definition of the onset – as the intersection of the steepest tangent of the peak with the baseline – is clearly inaccurate. $T_{c(onset)}$ is instead defined here as the temperature at which there is a noticeable deviation from the baseline

Table S4. Transition onset and peak temperatures for $[S_{(5)1}][FSI]$ at various pressures, determined from HP-DTA experiments. Values of ΔT_{hys} correspond to the difference between the onset temperatures of $T_{s\text{-}s}$ and T_c.

Pressure / bar	$T_{s\text{-}s}$ (onset) / °C	$T_{s\text{-}s}$ (peak) / °C	T_c (onset) / °C	T_c (peak) / °C	ΔT_{hys} / °C
1	-18.3	-17.7	-24.1	-21.2	5.8
105	-17.1	-16.3	-19.6	-18.8	2.5
200	-16.4	-15.8	-18.3	-18.2	1.9
298	-15.5	-14.8	-20.8	-18.8	5.3
395	-14.7	-14.0	-22.5	-17.0	7.8
425	-14.4	-13.6	-	-	-

542	-13.1	-12.3	-19.4	-15.3	6.3
652	-12.0	-11.2	-17.8	-15.2	5.8
				Average	5.0

*As $[S_{(5)1}][FSI]$ self-heats during crystallisation, the standard definition of the onset – as the intersection of the steepest tangent of the peak with the baseline – is clearly inaccurate. $T_{c(onset)}$ is instead defined here as the temperature at which there is a noticeable deviation from the baseline. Cooling data is not included for the scan at 425 bar due to a malfunction with the cooling device.

Table S5. Transition onset and peak temperatures for $[S_{(5)2}][FSI]$ at various pressures, determined from HP-DTA experiments. Values of ΔT_{hys} correspond to the difference between the onset temperatures of $T_{s\text{-}s}$ and T_c.

Pressure / bar	**$T_{s\text{-}s}$ (onset) / °C**	**$T_{s\text{-}s}$ (peak) / °C**	**T_c (onset) / °C**	**T_c (peak) / °C**	**ΔT_{hys} / °C**
1	-4.3	-2	-35.7	-15.4	31.4
125	-2.6	-5.5	-31.2	-11.4	28.6
295	-0.5	1.4	-23.1	-5.3	22.6
465	1.6	3.4	-23.7	-5.1	25.3
569	2.8	*4.5*	-22.5	-4.1	25.3
647	3.6	5.3	-25.6	-5.7	29.2
				Average	27.1

*As $[S_{(5)2}][FSI]$ self-heats during crystallisation, the standard definition of the onset – as the intersection of the steepest tangent of the peak with the baseline – is clearly inaccurate. $T_{c(onset)}$ is instead defined here as the temperature at which there is a noticeable deviation from the baseline.

Table S6. Transition onset and peak temperatures for $[N_{1111O1}][FSI]$ at various pressures, determined from HP-DTA experiments. Values of ΔT_{hys} correspond to the difference between the onset temperatures of $T_{s\text{-}s}$ and T_c.

Pressure / bar	**$T_{s\text{-}s}$ (onset) / °C**	**$T_{s\text{-}s}$ (peak) / °C**	**T_c (onset) / °C**	**T_c (peak) / °C**	**ΔT_{hys} / °C**
1	-8.2	-7.5	-17.3	-10.1	9.1
140	-6.1	-5.2	-16.4	-8.4	10.3
225	-4.1	-3.2	-14.5	-7.9	10.3
340	-3.2	-2.4	-13.5	-6.0	10.3
485	-1.0	-0.1	-10.8	-3.6	9.7
570	0.1	1.1	-8.8	-1.0	8.9
640	1.3	2.3	-8.3	-2.0	9.6
				Average	9.8

*As $[N_{1111O1}][FSI]$ self-heats during crystallisation, the standard definition of the onset – as the intersection of the steepest tangent of the peak with the baseline – is clearly inaccurate. $T_{c(onset)}$ is instead defined here as the temperature at which there is a noticeable deviation from the baseline.

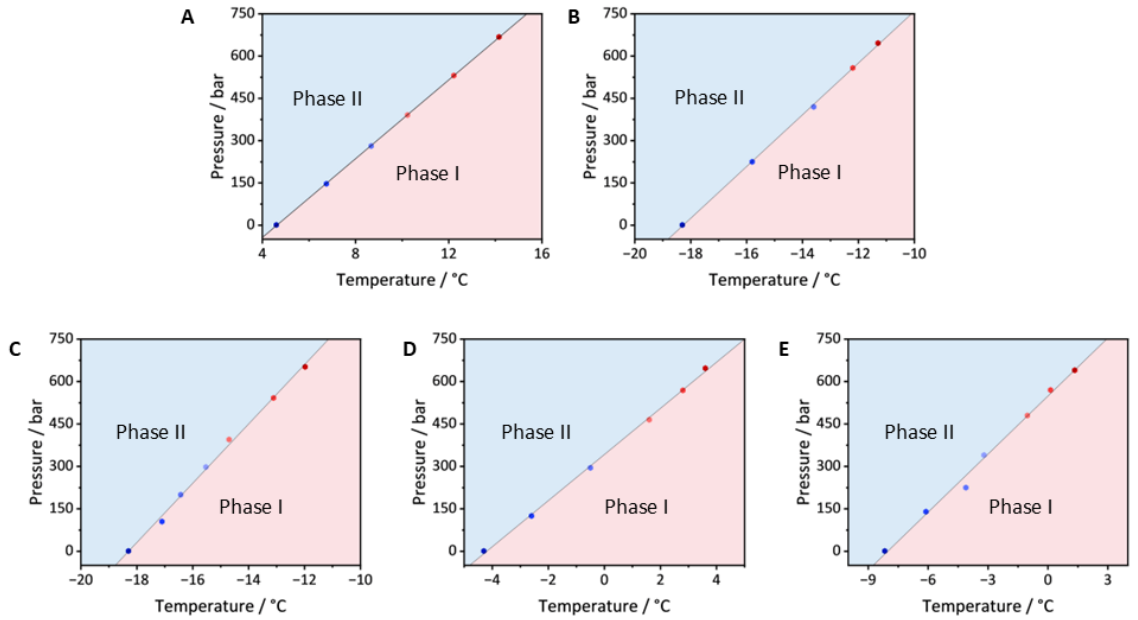

Figure S1. Phase diagrams of [S_{111}][FSI] (**A**), [S_{112}][FSI] (**B**), [$S_{(5)1}$][FSI] (**C**), [$S_{(5)2}$][FSI] (**D**), and [N_{1111O1}][FSI] (**E**), derived from the onset of the endothermic transitions in high-pressure thermal analysis conducted at various isobaric pressures between 1 and 700 bar. The datapoints are coloured to match the corresponding isobaric pressures in Figure 3 in the manuscript.

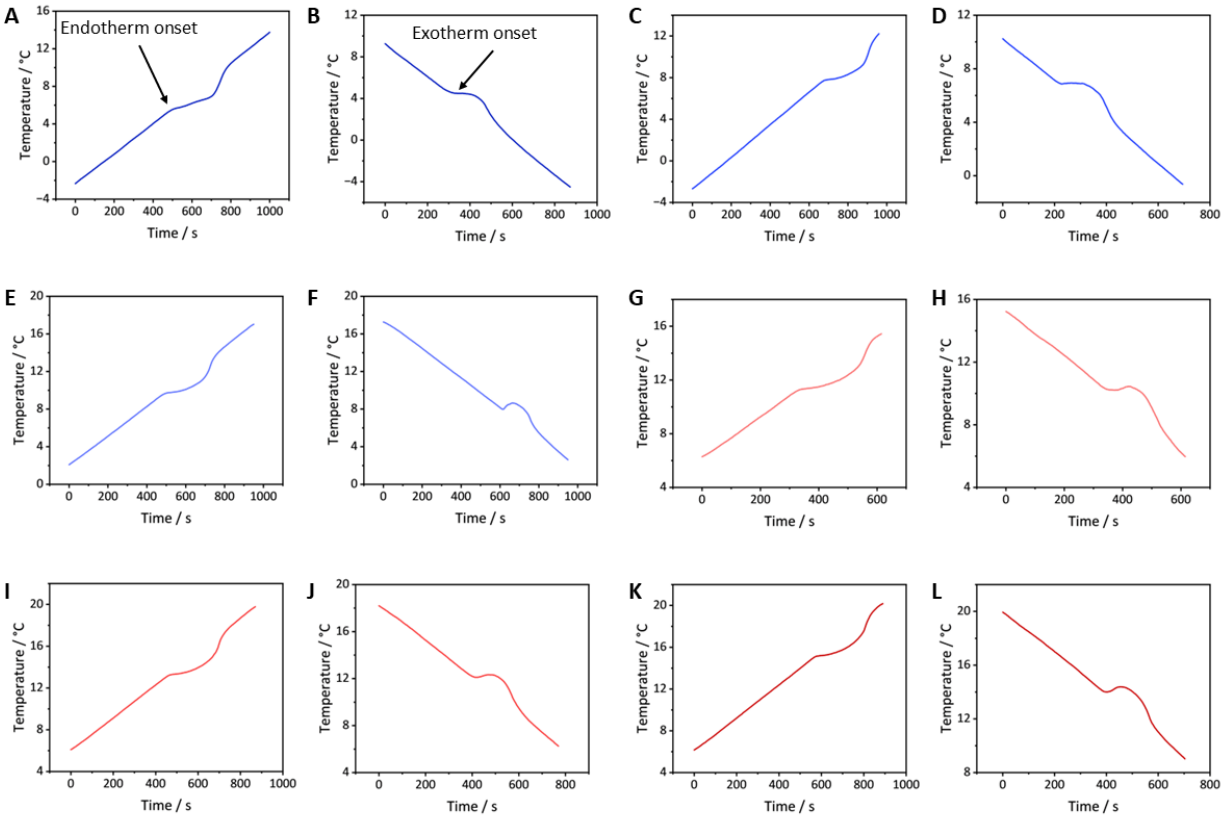

Figure S2. High pressure differential thermal analysis sample temperature vs time curves of [S_{111}][FSI]. (**A**) heating and (**B**) cooling at 1 bar; (**C**) heating and (**D**) cooling at 147 bar; (**E**) heating and (**F**) cooling at 281

bar; (**G**) heating and (**H**) cooling at 391 bar; (**I**) heating and (**J**) cooling at 531 bar; (**K**) heating and (**L**) cooling at 668 bar.

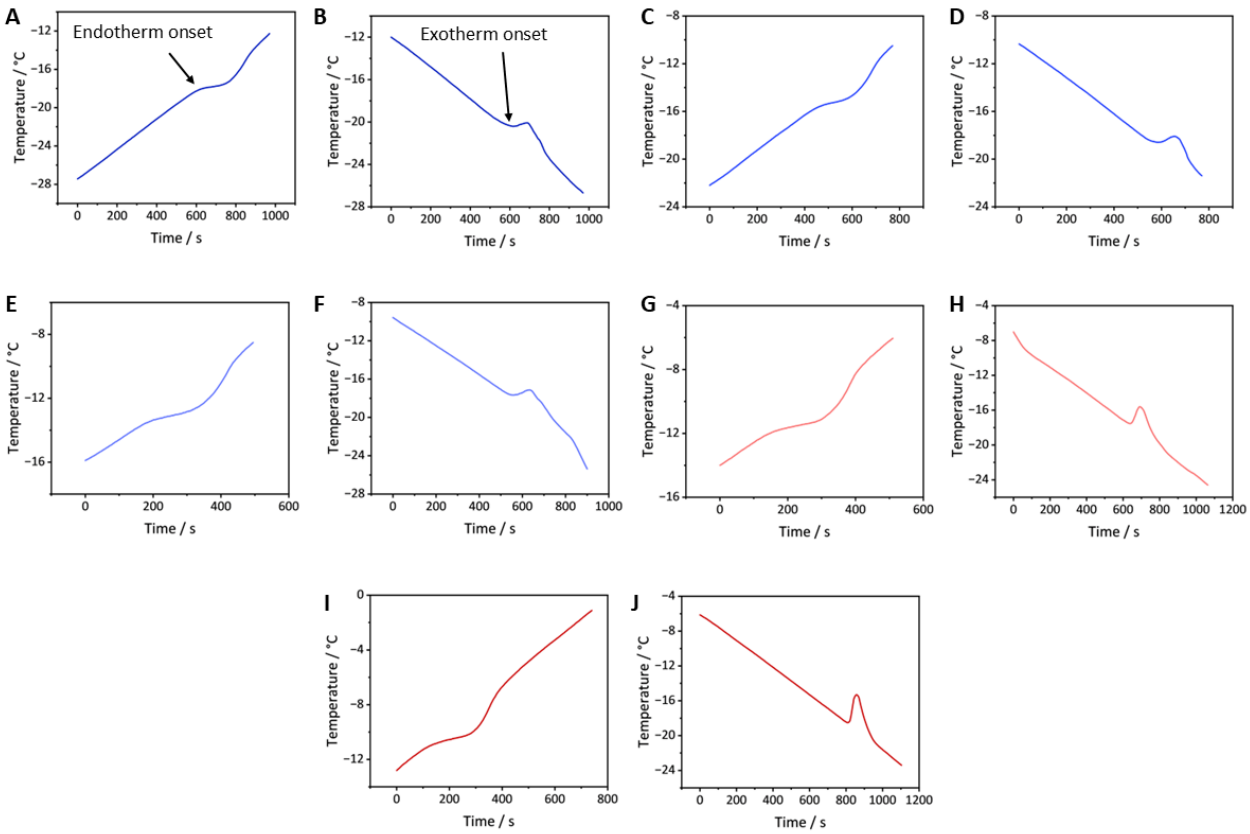

Figure S3. High pressure differential thermal analysis sample temperature vs time curves of [S_{112}][FSI]. (**A**) heating and (**B**) cooling at 1 bar; (**C**) heating and (**D**) cooling at 225 bar; (**E**) heating and (**F**) cooling at 420 bar; (**G**) heating and (**H**) cooling at 558 bar; (**I**) heating and (**J**) cooling at 646 bar.

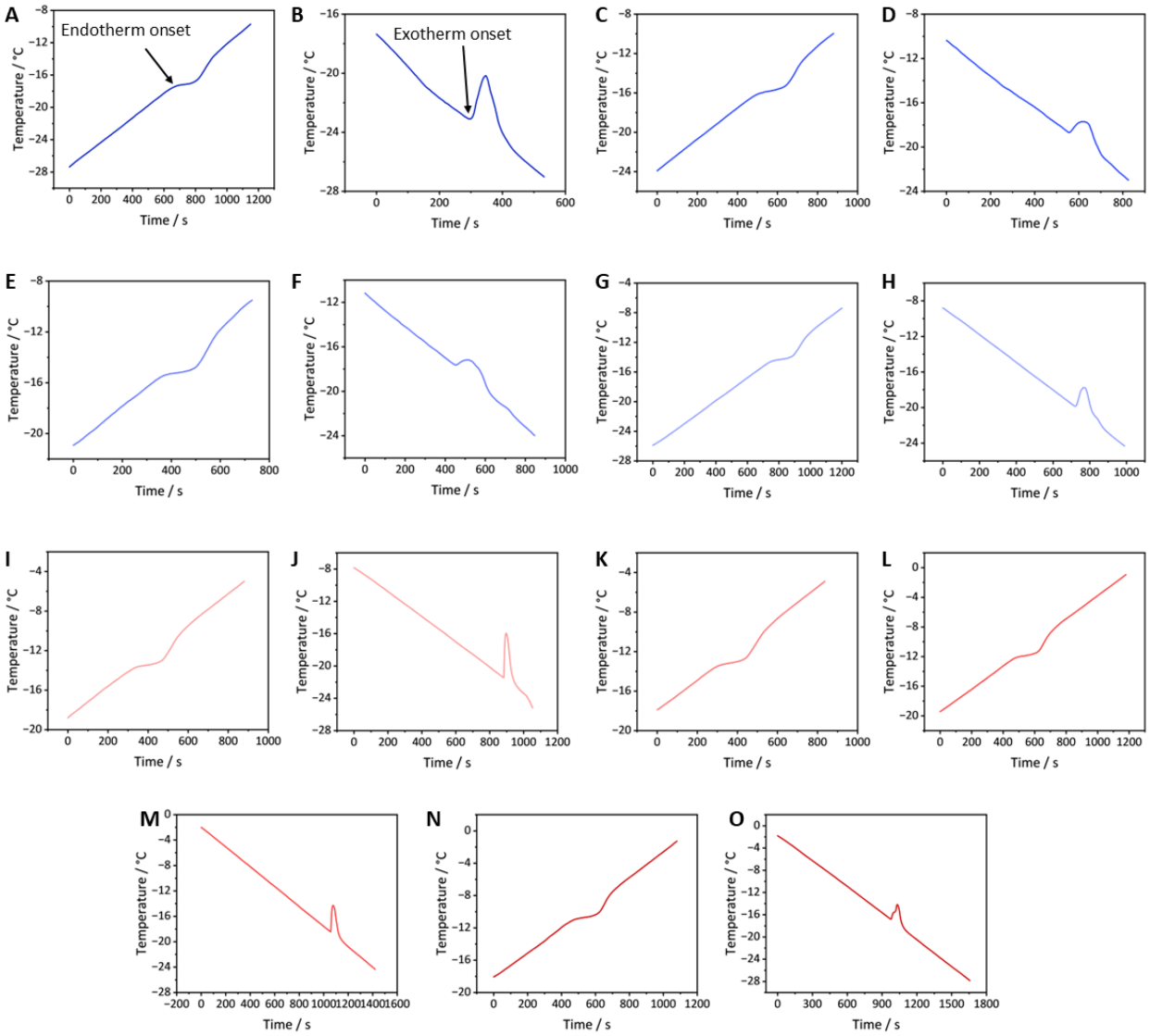

Figure S4. High pressure differential thermal analysis sample temperature vs time curves of [$S_{(5)1}$][FSI]. (**A**) heating and (**B**) cooling at 1 bar; (**C**) heating and (**D**) cooling at 105 bar; (**E**) heating and (**F**) cooling at 200 bar; (**G**) heating and (**H**) cooling at 298 bar; (**I**) heating and (**J**) cooling at 395 bar; (**K**) heating at 425 bar; (**L**) heating and (**M**) cooling at 542 bar; (**N**) heating and (**O**) cooling at 652 bar.

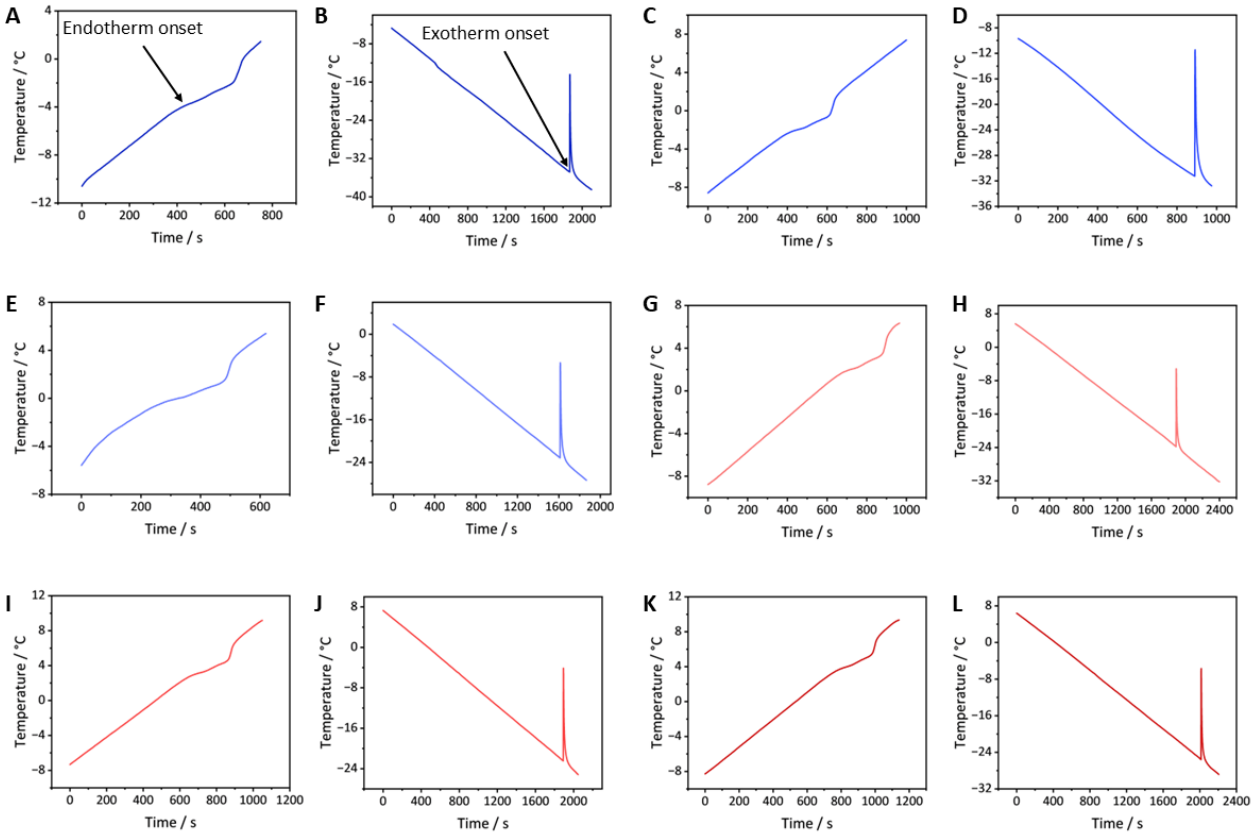

Figure S5. High pressure differential thermal analysis sample temperature vs time curves of $[S_{(5)2}][FSI]$. (**A**) heating and (**B**) cooling at 1 bar; (**C**) heating and (**D**) cooling at 125 bar; (**E**) heating and (**F**) cooling at 295 bar; (**G**) heating and (**H**) cooling at 465 bar; (**I**) heating and (**J**) cooling at 569 bar; (**K**) heating and (**L**) cooling at 647 bar.

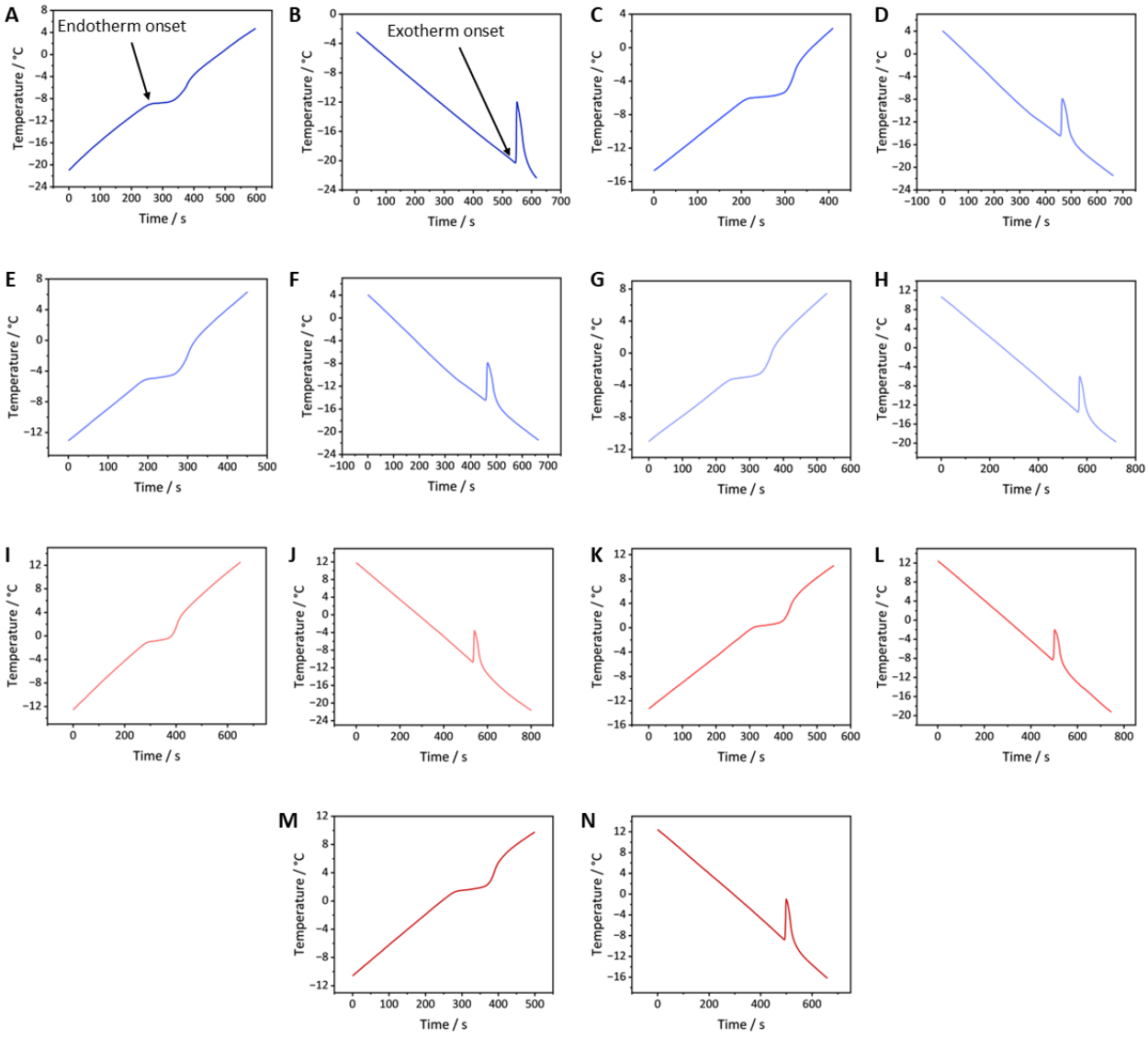

Figure S6. High pressure differential thermal analysis sample temperature vs time curves of [N_{1111O1}][FSI]. (**A**) heating and (**B**) cooling at 1 bar; (**C**) heating and (**D**) cooling at 140 bar; (**E**) heating and (**F**) cooling at 225 bar; (**G**) heating and (**H**) cooling at 340 bar; (**I**) heating and (**J**) cooling at 485 bar; (**K**) heating and (**L**) cooling at 570 bar; (**M**) heating and (**N**) cooling at 640 bar.

Pressure cycling

To confirm the cycling stability of the solid-solid transitions during the application-relevant pressure cycles, [S_{111}][FSI] was chosen as a representative OIPC and subjected to 100 pressure cycles in the DTA. The sample was maintained at a temperature between 6.5 and 7 °C (2-3 °C above the transition temperature at ambient pressure). Pressure was applied manually using a hydraulic pump, at a rate of ~150 bar min^{-1}, until the temperature of the sample was observed to increase at a faster rate than that of the reference material, which indicated that the material was crystallising. This approach allows for the requirement for an additional pressure (ΔP_{hys}) which is required to initiate the formation of the new phase, equivalent to the ΔT_{hys} in the isobaric experiments. The system was then maintained at this pressure for ~4 minutes to allow the material time to fully crystallise. The pressure was then released rapidly, causing a small drop in temperature within the system. In equilibrating back to the set temperature, the lag in sample

temperature relative to the reference material was indicative of the endothermic transition from the pressure induced phase II to phase I. The data was plotted as Δ*T* vs time, where Δ*T* is the difference in temperature between the sample and reference material (see Figure S7). The integration of Δ*T* vs time is representative of the heat absorbed by the sample during the endothermic transition. Thus, the consistency of this integration over the 100 cycles (Figure S8A) confirms the material retains the magnitude of its entropy change over the 100 cycles. Similarly, we observe the exothermic transition to occur at a consistent pressure over the 100 cycles, Figure S8B, confirming the material retains its remarkably low hysteresis over the 100 cycles. This indicates that there is no pressure induced degradation of the sample occurring. This cycling stability was further confirmed by conducting a DTA heating scan at ambient pressure (scan rate 1 °C min^{-1}) after cycling, which was compared to the equivalent heating scan conducted on the material before the pressure cycling (Figure S9). The consistency of the onset temperature and integration of the endothermic transition before and after cycling indicates no degradation occurred in the sample during the cycling experiment.

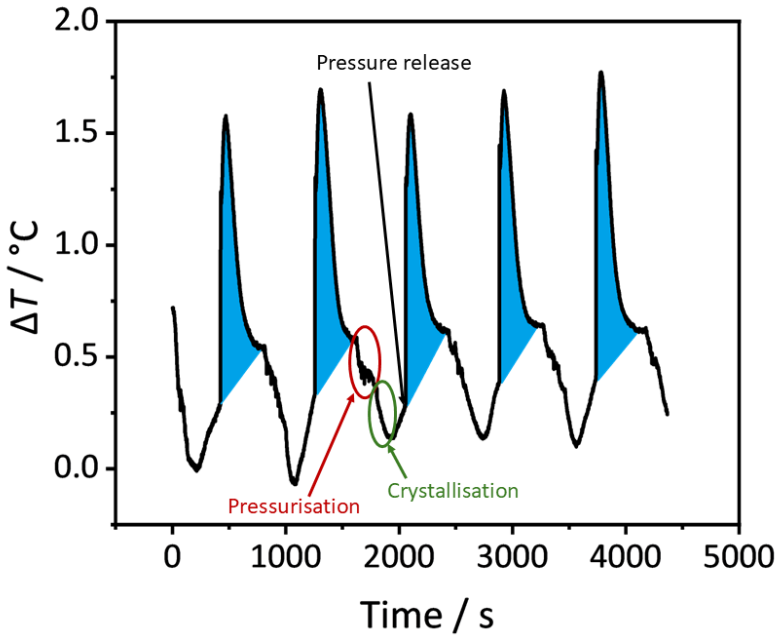

Figure S7. Representative pressure cycles of $[S_{111}][FSI]$ from the 100 pressure cycles conducted on the material. The graph is annotated to demonstrate the regions in which pressure is applied and released, and the region in which the pressure induced crystallisation from phase I-II occurs. The regions corresponding to the endothermic phase II-I transition upon pressure release, for which the integration represents total heat flow into the material, are shaded blue. The consistency of the integration of this blue shaded region over the 100 cycles (Figure S8A) confirms no changes occur to the magnitude of the transition over the 100 cycles.

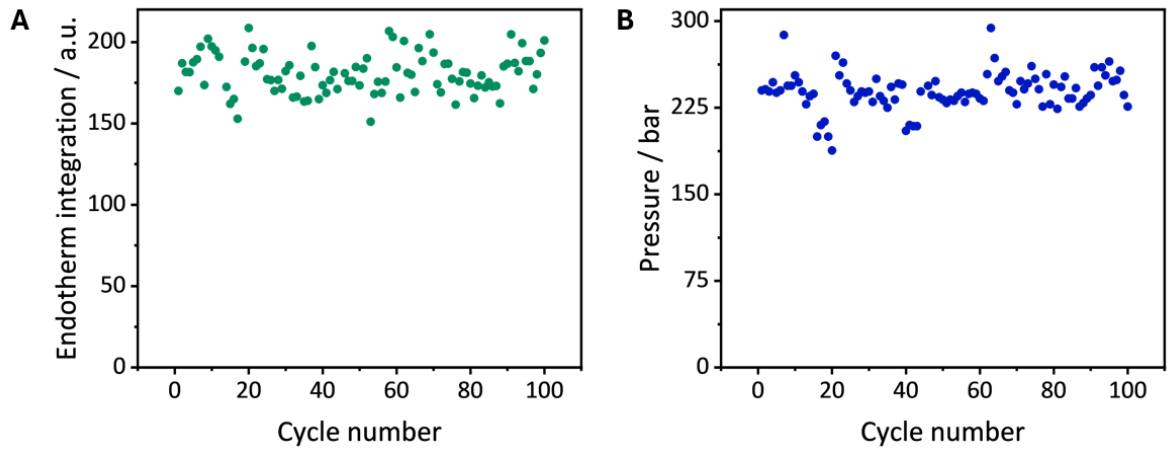

Figure S8. DTA pressure cycling of $[S_{111}][FSI]$. (**A**) Integration of ΔT vs time during the phase II-I transition upon depressurisation, representative of the heat absorbed by the material during the endothermic transition. One datapoint (cycle 13) was identified as an outlier, falling more than 1.5 x IQR below the first quartile, and was removed from the dataset. (**B**) Pressure at which the pressure-induced phase I-II transition was observed while the temperature of the sample was maintained at ~7 °C (~3 °C above the temperature of the endothermic transition at ambient pressure). The consistency of the integration and pressure values in **A** and **B** indicates no pressure-induced degradation occurs in the sample over the 100 cycles.

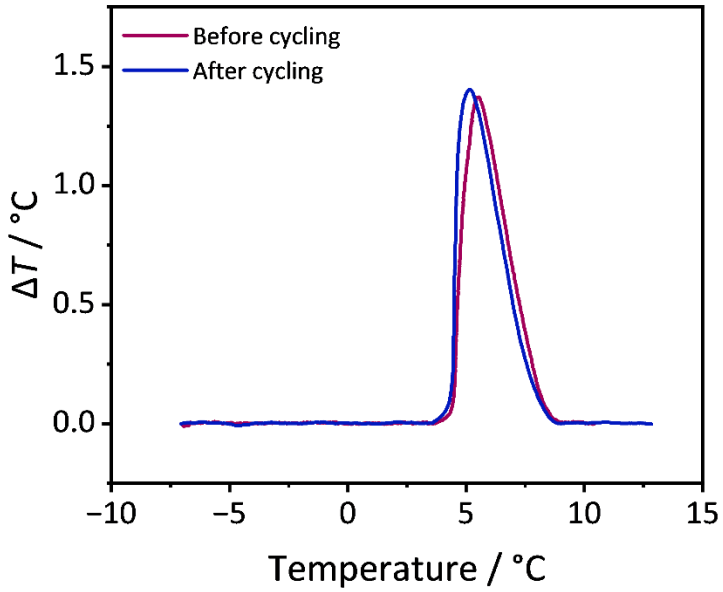

Figure S9. Isobaric DTA curves of $[S_{111}][FSI]$ during heating at ambient pressure before (purple) and after (blue) 100 pressure cycles. The consistency of the onset temperature and relative integration of the endothermic transition indicates that no pressure induced degradation has occurred in the sample over the 100 pressure cycles.

Differential scanning calorimetry

Phase transition temperatures ($T_{s\text{-}s}$, T_m) and enthalpies ($\Delta H_{s\text{-}s}$, ΔH_m) were determined by differential scanning calorimetry using a Netzsch 300 Caliris calorimeter (scan rate of 10 °C min^{-1}). Approximately ~5 mg of sample was hermetically sealed in an aluminium pan for the analysis.

Thermal cycling

To confirm the of thermal cyclability of the solid-solid transitions, 100 heating/cooling cycles of $[S_{111}][FSI]$ were conducted by DSC using a Netzsch 300 Caliris calorimeter with a ramp rate of 10 °C min^{-1} (sample mass 10.6 mg). The entropy change of the endothermic phase II-I was found to be consistent over the 100 cycles (Figure S10B).

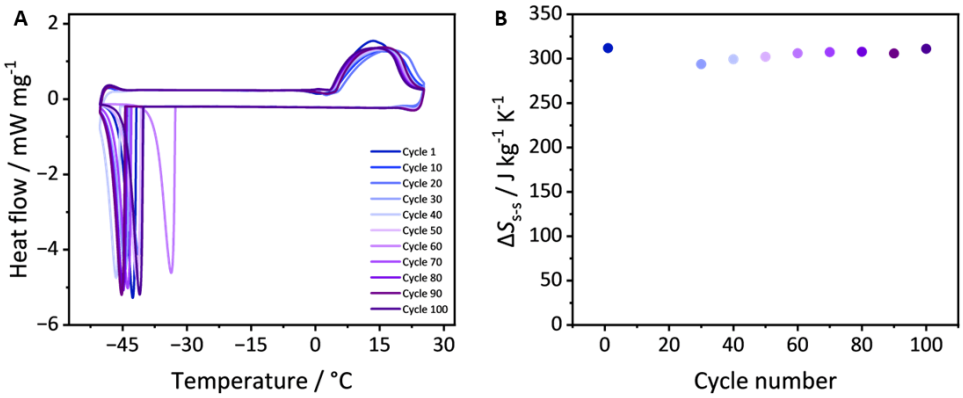

Figure S10. (**A**) Representative heating and cooling DSC cycles of $[S_{111}][FSI]$ from the 100 thermal cycles conducted on the material (scan rate of 10 °C min^{-1}). (**B**) Entropy change, $\Delta S_{s\text{-}s}$, of the representative cycles shown in A. The consistency of $\Delta S_{s\text{-}s}$ across the 100 cycles indicates no degradation occurs in the material during the 100 DSC cycles. Values of $\Delta S_{s\text{-}s}$ are missing for cycles 10 and 20 as the heat flow had not returned to baseline before the cooling cycle begun and thus the integration of the peak, which is used to calculate $\Delta S_{s\text{-}s}$, is not reliable.

Heat capacity determination

The heat capacities (C_p) of the OIPCs were determined using a Netzsch 300 Caliris DSC calorimeter. The heat capacity of each sample was determined from three separate DSC scans using a heating rate of 1 °C min^{-1} over the temperature range of interest (approximately 40 °C on either side of $T_{s\text{-}s}$). The first scan was conducted on an empty aluminium sample pan to determine the baseline; the second scan was conducted on the same sample pan, containing a 25 mg sapphire disc standard, to calibrate the heat capacity; the third scan was conducted on 20-40 mg of the sample.

Table S7. Linear fits of the heat capacity measurements of the OIPCs in phase I and phase II from the calibrated DSC thermograms (**Figure S11**), determined using a scan rate of 1 °C min^{-1}.

OIPC	Phase II				Phase I			
	m	±	c	±	m	±	c	±
[S_{111}][FSI]	0.00409	0.000367	0.9961	0.00963	0.00302	0.000424	1.01027	0.01148
[$S_{(5)1}$][FSI]	0.00688	0.000440	1.12691	0.01854	0.00273	0.000395	1.26541	0.00567
[N_{1111O1}][FSI]	0.00814	0.0002094	1.19831	0.00857	0.03113	0.0023	1.34658	0.05652
[$S_{(5)2}$][FSI]	0.00317	0.00049306	1.10486	0.0129	0.00058	0.000778	1.19669	0.01496
[S_{112}][FSI]	0.00204	0.0005281	0.78424	0.01598	0.0058	0.000754	1.09873	0.00435

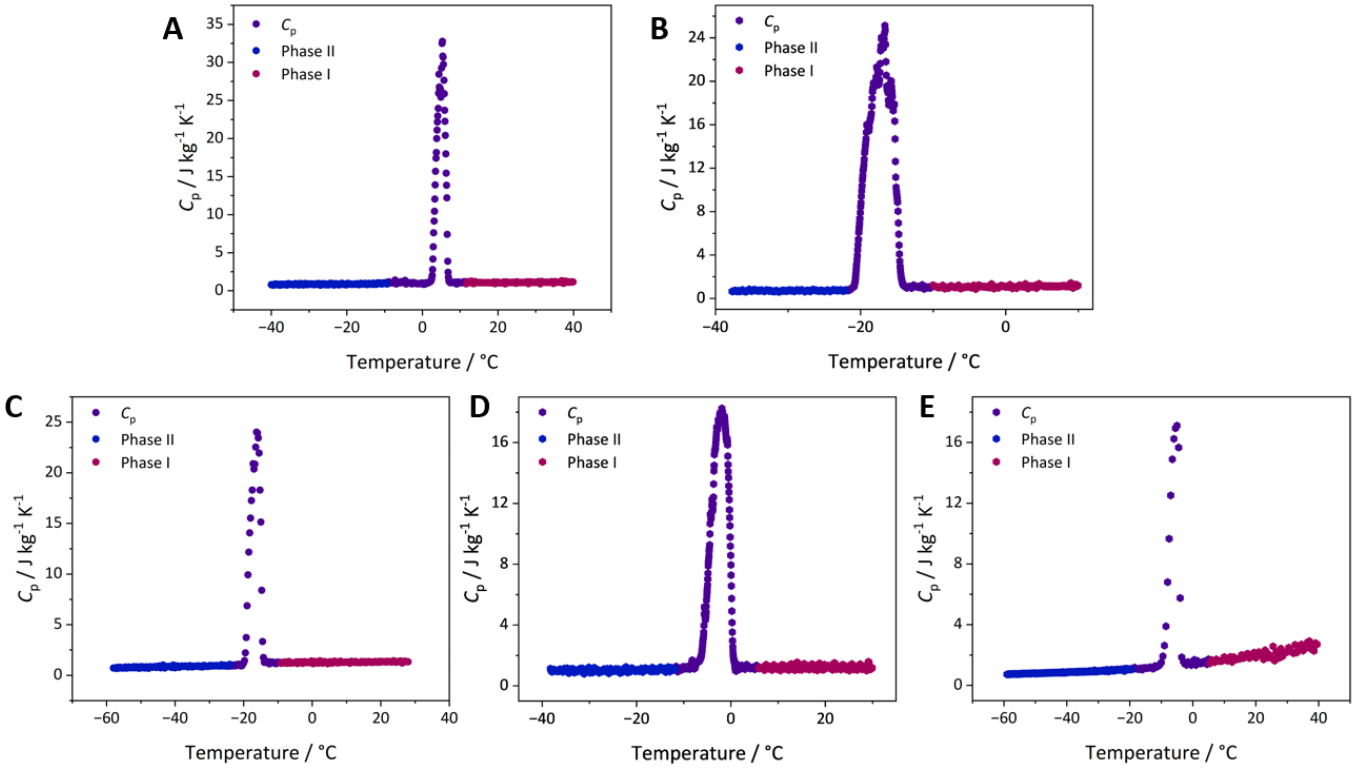

Figure S11. Calibrated heat capacity (C_p) DSC thermogram for [S_{111}][FSI] (**A**), [S_{112}][FSI] (**B**), [$S_{(5)1}$][FSI] (**C**), [$S_{(5)2}$][FSI] (**D**) and [N_{1111O1}][FSI] (**E**), determined using a scan rate of 1 °C min^{-1}. The linear fits of C_p in phase I (blue dots) and phase II (pink dots) are provided in **Table S7**.

1.3 Volume change determination

The volume changes associated with the transitions ($\Delta V_{s\text{-}s}$) were calculated from the measured values of $dT_{s\text{-}s}/dp$ (from HP-DTA) and $\Delta S_{s\text{-}s}$, via the Clausius-Clapeyron relationship:

$$\Delta V_{s-s} = \left(\frac{dT_{s-s}}{dp}\right) \times \Delta S_{s-s}$$

To validate the values from this calculation, we measured $\Delta V_{s\text{-}s}$ for three of the OIPCs ([S_{111}][FSI], [$S_{(5)1}$][FSI] and [N_{1111O1}][FSI]) using a solvent displacement pycnometric method that we have previously reported.[2] In summary, a known mass of OIPC (~0.5 g – 1 g) was placed into a 1 mL conical flask to which a ~1 mm capillary could be attached via a ground glass joint. The flask was filled with silicone oil ((-Si(CH_3)$_2$O-)n, ρ = 0.963 g mL^{-1} at 25 °C, sourced from Sigma-Aldrich) at ambient temperature and the vessel was agitated to ensure no bubbles were present. The flask was then cooled to a temperature substantially below the $T_{s\text{-}s}$ of the respective OIPC to ensure crystallisation into the low temperature phase had occurred. The vessel was topped up with silicone oil and the capillary was attached to the top of the flask, which was then immersed (up to the joint) in a chilled bath held at a constant temperature, ~10 °C below $T_{s\text{-}s}$. The vessel was equilibrated at this starting temperature for at least 30 minutes, and silicone oil ejected from the capillary due to thermal expansion was removed. Hence, after the system had equilibrated, the vessel was perfectly full at the starting temperature. The temperature of the bath was then increased at a rate of 1 °C every six minutes, during which time the silicone oil ejected from the capillary (due to thermal expansion of both the contained OIPC and silicone oil) was collected and weighed. The mass ejected was converted to a volume using the below equation for the density of silicone oil vs temperature (determined in our previous work[2]), which was graphed against temperature. The volume change of the transition was represented by a deviation from the linear trend of ejected oil. Following completion of the transition, the rate of expulsion of silicone oil returned to a linear trend, again attributed to the thermal expansion of the silicone oil and the OIPC, now in the plastic phase (phase I). To determine the volume of silicone oil expelled due to the OIPC transition, the equations of the linear fits before and after (**Table S8**) the transition were solved where x = $T_{s\text{-}s}$. The discrepancy between the two values is equal to the change in specific volume, $\Delta\nu_{s\text{-}s}$, in m^3 kg^{-1}.

$$p_{(Si\ oil)} = -0.000912(T) + 0.9813$$

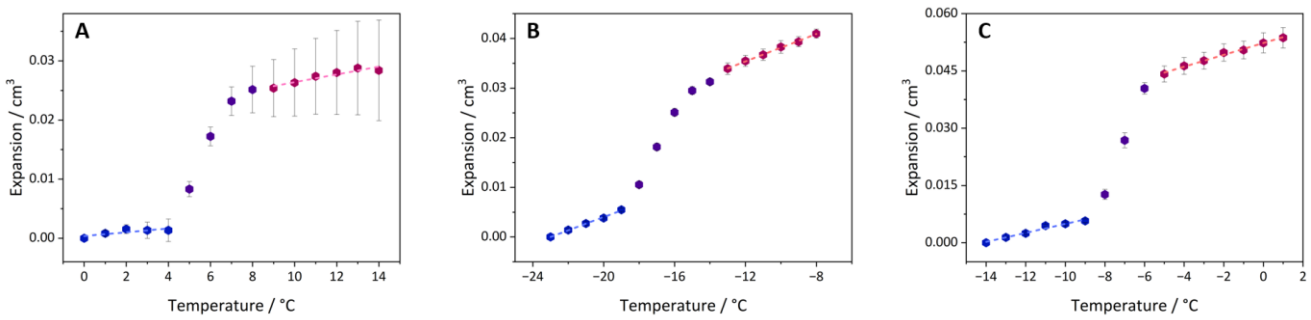

Figure S12. Solvent displacement data for 0.5514 g [S_{111}][FSI] (**A**), 0.7118 g [$S_{(5)1}$][FSI] (**B**) and 0.9113 g [N_{1111O1}][FSI] (**C**). The linear fits of solvent expulsion before and after the transition were solved for x = $T_{s\text{-}s}$, and the discrepancy between the values is equal to the volume change of the material at the transition. All data points indicate the average of at least triplicates (**Table S8**).

Table S8. Features of the linear lines of best fit for the volume change experiments conducted on the OIPCs using the solvent expulsion pycnometric method.

OIPC		Phase II				Phase I						
	Run	Gradient $cm^3/°C$	±	Y-int cm^3	±	Gradient $cm^3/°C$	±	Y-int cm^3	±	ΔV / cm^3	Δv_{s-s} / m^3/kg	Predicted dT_{s-s}/dp K $kbar^{-1}$
$[S_{111}][FSI]$ 0.5514 g	**1**	0.0015	0.0002	0.0008	0.0006	0.0009	0.0001	0.0252	0.0007	0.022	4.0×10^{-5}	13.5
	2	0.0024	0.0001	-0.0004	0.0003	0.0035	0.0001	0.0139	0.0017	0.019	3.4×10^{-5}	11.5
	3	0.0003	0.0001	0.0004	0.0003	0.0006	0.0001	0.0195	0.0013	0.020	3.7×10^{-5}	12.5
	Avg	0.0014	0.0002	0.0002	0.0004	0.0017	0.0001	0.0195	0.0012	0.020	3.7×10^{-5}	12.5
$[S_{(5)1}][FSI]$ 0.7118 g	**1**	0.0016	0.0001	0.0365	0.0015	0.0015	0.0001	0.0548	0.0007	0.020	2.9×10^{-5}	9.0
	2	0.0013	0.0001	0.0292	0.0026	0.0013	0.0001	0.0484	0.0010	0.018	2.6×10^{-5}	8.1
	3	0.0011	0.0002	0.0262	0.0051	0.0010	0.0001	0.0500	0.0013	0.026	3.6×10^{-5}	11.4
	4	0.0014	0.0001	0.0313	0.0015	0.0017	0.0001	0.0547	0.0007	0.017	2.4×10^{-5}	7.4
	Avg	0.0013	0.0001	0.0308	0.0027	0.0014	0.0001	0.0520	0.0009	0.020	2.9×10^{-5}	9.0
$[N_{1111O1}][FSI]$ 0.9113 g	**1**	0.0014	0.0001	0.0200	0.0011	0.0022	0.0001	0.0579	0.0002	0.032	3.5×10^{-5}	13.9
	2	0.0010	0.0001	0.0142	0.0008	0.0017	0.0000	0.0474	0.0002	0.028	3.1×10^{-5}	12.2
	3	0.0011	0.0002	0.0160	0.0019	0.0008	0.0002	0.0516	0.0005	0.038	4.2×10^{-5}	16.9
	Avg	0.0012	0.0001	0.0167	0.0012	0.0016	0.0001	0.0523	0.0002	0.033	3.6×10^{-5}	14.3

1.4 Nuclear Magnetic Resonance (NMR) Spectroscopy

Liquid-state NMR

NMR spectra were recorded at 298 K on a Bruker Avance III NMR spectrometer equipped with a 9.4 T magnet and 5 mm TBO probe, operating at 400.13 MHz (^{1}H). Chemical shifts (δ) are reported in parts per million (ppm) and were referenced to the residual solvent signals (^{1}H, ^{13}C) or from the solvent block (^{2}H) signal according to IUPAC recommended secondary referencing method and the manufacturer's protocols (^{19}F).

Static solid-state ^{1}H and ^{19}F NMR

Static solid-state ^{1}H and ^{19}F NMR experiments were conducted on a Bruker Avance III wide-bore spectrometer equipped with a 11.7 T magnet and 5 mm static HX variable-temperature probe, operating at 300.12 MHz (^{1}H frequency). Samples were packed in a 5 mm glass tube, and the spectra were recorded with single-pulse excitation over 32 scans with a relaxation delay of 5 seconds and pulse width of 3 µs. Frequency scales were referenced to the signal of a tetramethylsilane standard (0 kHz). Spectra were

analysed using Topspin and deconvolution fitting was done with the DMfit software. Examples of the deconvoluted spectra for those that were modelled as multi-component are shown in Figure S14 – S17.

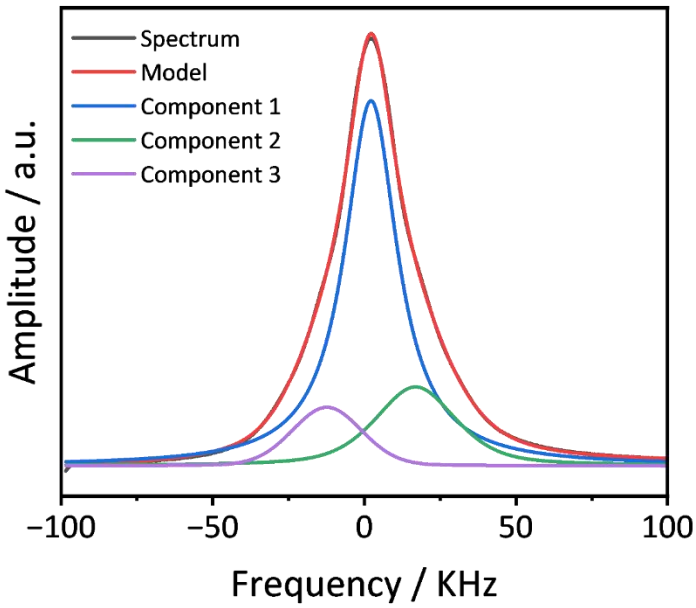

Figure S13. Static solid-state ^{1}H NMR spectrum of [S_{112}][FSI] at -50 °C, showing the three-component model (deconvoluted using DMFit software).

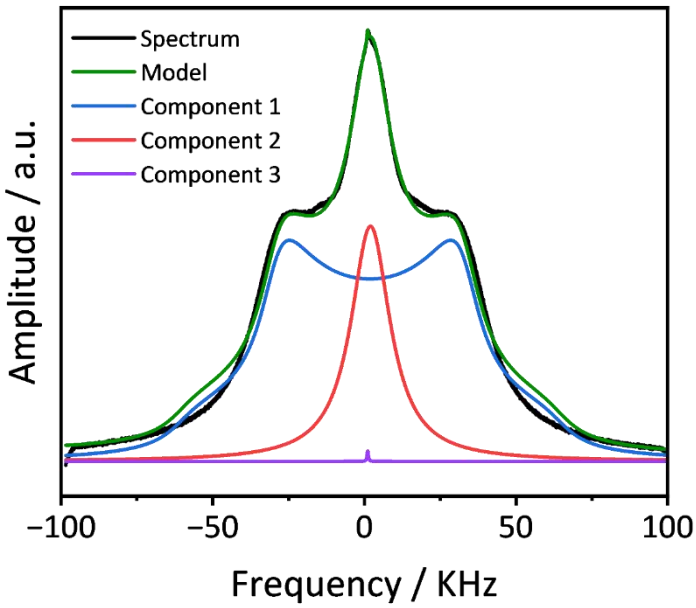

Figure S14. Static solid-state ^{1}H NMR spectrum of [$S_{(5)1}$][FSI] at -40 °C, showing the three-component model (deconvoluted using DMFit software).

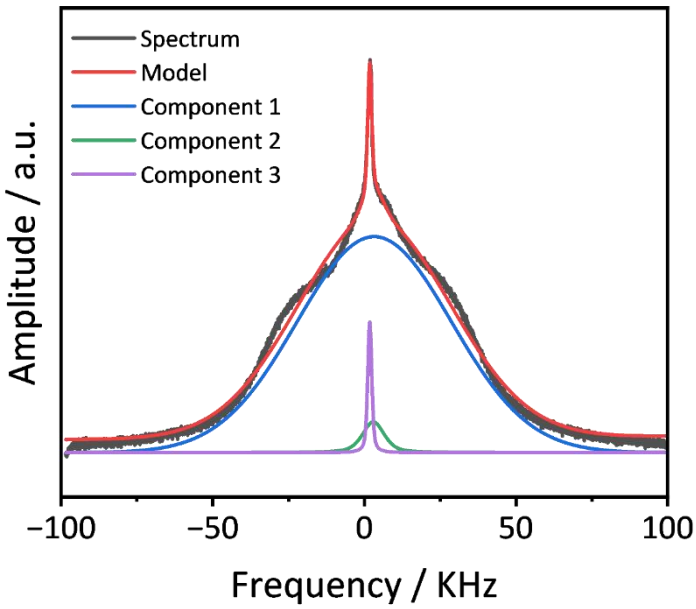

Figure S15. Static solid-state ^{1}H NMR spectrum of [$S_{(5)2}$][FSI] at -30 °C, showing the three-component model (deconvoluted using DMFit software).

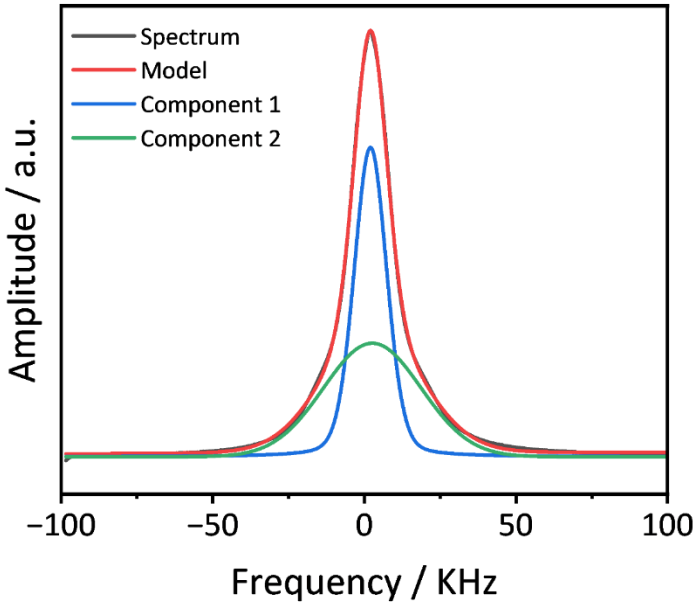

Figure S16. Static solid-state ^{1}H NMR spectrum of [N_{1111O1}][FSI] at -35 °C, showing the two-component model (deconvoluted using DMFit software).

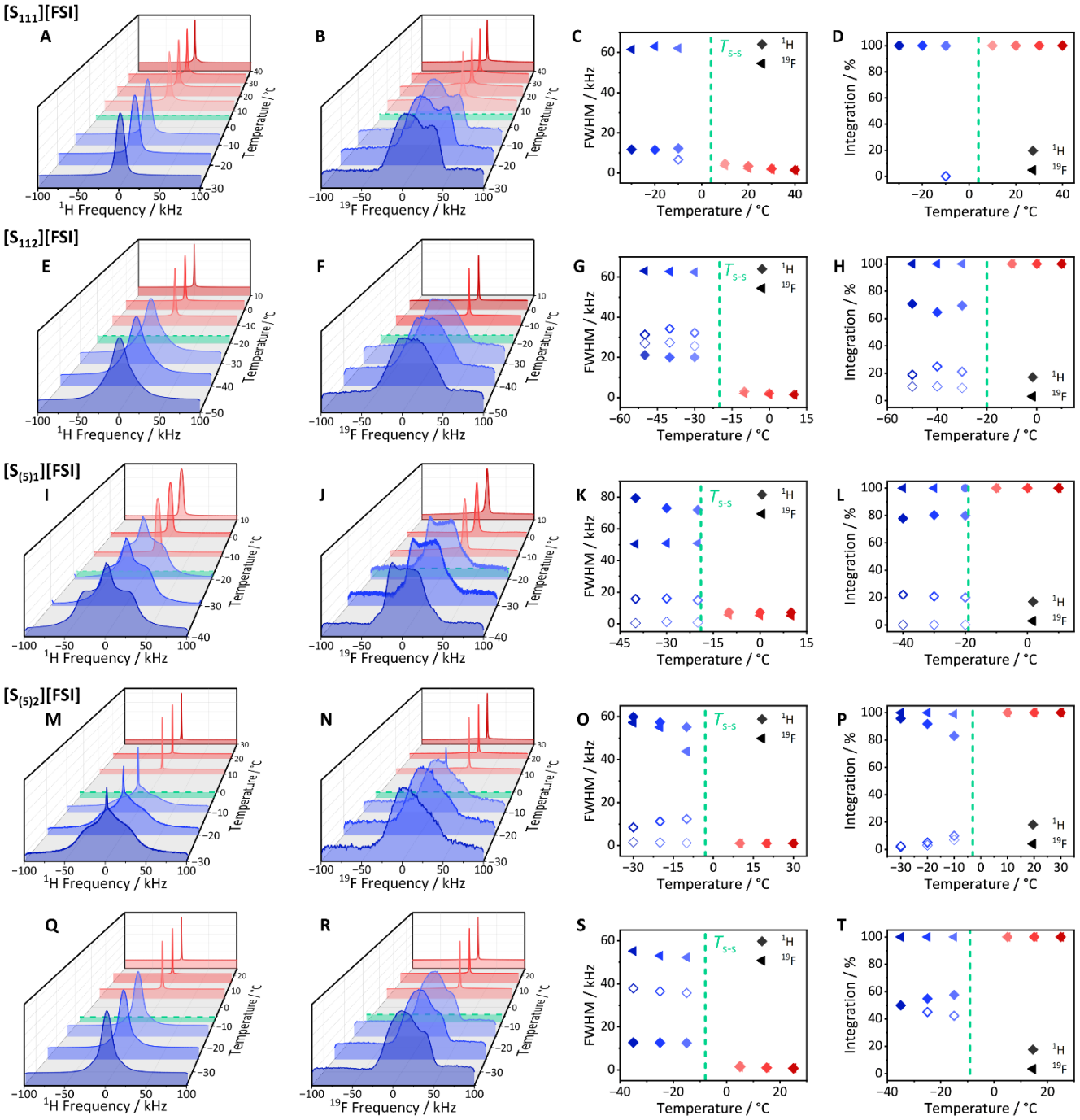

Figure S17. An expanded version of Fig 5 in the manuscript. Static solid-state ^{1}H NMR (first column) and ^{19}F NMR (second column) spectra of the BC OIPCs at various temperatures below and above their respective $T_{s\text{-}s}$ ($T_{s\text{-}s}$ are represented by the dashed green lines). The FWHM of the components of the deconvoluted spectra are plotted in the third column, with ^{1}H diamonds and ^{19}F as triangles. When multiple components are observed, the second and third components are plotted as hollow symbols. The relative integrations of the various components are plotted in the fourth column.

Supplementary static-solid state NMR discussion (expanded version of the discussion in the manuscript)

The ^{19}F NMR spectra of the OIPCs below their respective $T_{s\text{-}s}$ all show a signal consistent with a dynamically averaged chemical shift anisotropy (CSA) peak, indicating the $[FSI]^-$ anions are relatively static. In all cases, the full width at half-maximum (FWHM) of these signals is relatively constant or decreases gradually with increasing temperature up to $T_{s\text{-}s}$ (i.e. in phase II), before a narrow, symmetric component emerges in the spectra above $T_{s\text{-}s}$ (in phase I). The FWHM of the NMR signals in the phase I spectra are substantially reduced compared to those of the phase II CSA signals; this indicates a sharp increase in anion dynamics at the transition.

More diversity of line shapes is observed between the ^{1}H NMR spectra of the OIPCs due to the different cation structures. The spectra of the cyclic sulfonium cations $[S_{(5)1}]$ and $[S_{(5)2}]$ in phase II are both modelled as three-components (**Figure S14** and **Figure S15**); one broad (FWHM ~ 50 – 60 kHz), one moderate (~ 15 kHz for $[S_{(5)1}]$ and ~ 10 kHz for $[S_{(5)2}]$), and one narrow (~ 1 kHz for both), indicating the coexistence of three different cation environments in each OIPC. The broader components are attributed to less mobile ions in more ordered, crystalline regions, while the FWHM of the narrow components is attributed to ions exhibiting translational motions.[3] While the narrow component accounts for less than 1% of the integration of the signal in the $[S_{(5)1}]$ spectra, the narrow component in $[S_{(5)2}]$ increases from ~2% at -30 °C to ~ 7% at -10 °C. Conversely, the moderate-width component (likely representing a population of cations with intermediate mobility, e.g. vibrations or sluggish rotations) has a higher relative integration in $[S_{(5)1}]$ when compared to $[S_{(5)2}]$, consistently around 20% at all phase II temperatures, while that in the $[S_{(5)2}]$ spectra increases from ~2% to ~10% from -30 °C to -10 °C. Above $T_{s\text{-}s}$, the spectra of both $[S_{(5)1}]$ and $[S_{(5)2}]$ display only one component, with a FWHM of ~ 7 kHz for $[S_{(5)1}]$ and ~ 1 kHz for $[S_{(5)2}]$. The ^{1}H NMR spectra of $[N_{1111O1}]$ in phase II similarly shows a broad and moderate-width component (FWHMs ~36 kHz and ~12 kHz); an example of the fit is shown in **Figure S16**. These have an equal relative integration at -35 °C, while the integration of the moderate (more mobile) component increases at the expense of the broad component with increasing temperature until $T_{s\text{-}s}$, after which only one narrow component is observed with a FWHM of ~ 1 kHz. As with $[S_{(5)1}][FSI]$ and $[S_{(5)2}][FSI]$, this indicates the cations are highly mobile in the plastic phases of the salts and play a substantial role in the large values of $\Delta S_{s\text{-}s}$ observed for these salts.

The ^{1}H spectra of $[S_{111}][FSI]$ in both phases display only one, Gaussian-shaped peak, though a small, narrow component (FWHM = 6.61 kHz, relative integration 0.2%) arises in the highest temperature spectra below $T_{s\text{-}s}$ (-10 °C), indicating a small fraction of cations become mobile at this temperature. The FWHM of the main $[S_{111}]$ signal is consistently ~ 12 kHz at all temperatures below $T_{s\text{-}s}$; a sharp decrease in FWHM occurs over the transition, to 4.6 kHz (one component), which further decreases with increasing temperature in phase I to 1.5 KHz at 40 °C.

The ^{1}H spectra of $[S_{112}][FSI]$ in phase II is modelled as a three-component fit (**Figure S13**), where all components are relatively broad (FWHM = 20 – 45 kHz), indicating all of the cations are relatively immobile in this phase. As with the other OIPCs, only one narrow, Gaussian-shaped peak is observed in the phase I spectra (FWHM ~ 1.5 – 3 kHz), indicating a high level of cation mobility is introduced at the solid-solid phase transition in $[S_{112}][FSI]$.

Table S9. Full-width at half-maximum (FWHM) and relative integration of the components within the NMR signal in the ^{1}H NMR spectra of [S_{111}][FSI] at various temperatures above and below $T_{s\text{-}s}$ (presented in Fig 5 in the manuscript).

	Component 1		**Component 2**	
Temperature / °C	**FWHM / kHz**	**Integration / %**	**FWHM / kHz**	**Integration / %**
-30	11.7	100		
-20	11.5	100		
-10	12.2	99.8	6.6	0.2
10	4.6	100		
20	3.4	100		
30	2.1	100		
40	1.5	100		

Table S10. Full-width at half-maximum (FWHM) and relative integration of the components within the NMR signal in the ^{19}F NMR spectra of [S_{111}][FSI] at various temperatures above and below $T_{s\text{-}s}$ (presented in Fig 5 in the manuscript).

Temperature / °C	**FWHM / kHz**	**Integration / %**
-30	61.6	100
-20	63.1	100
-10	62.2	100
10	3.8	100
20	2.3	100
30	1.7	100
40	1.3	100

Table S11. Full-width at half-maximum (FWHM) and relative integration of the signal in the ^{1}H NMR spectra of [S_{112}][FSI] at various temperatures above and below $T_{s\text{-}s}$ (presented in Fig 5 in the manuscript).

	Component 1		**Component 2**		**Component 3**	
Temperature / °C	**FWHM / kHz**	**Integration / %**	**FWHM / kHz**	**Integration / %**	**FWHM / kHz**	**Integration / %**
-50	21.1	70.7	31.3	19.0	27.0	10.3
-40	20.0	64.6	34.3	25.0	27.4	10.4
-30	20.0	69.5	32.2	21.2	25.6	9.3
-10	3.0	100				
0	2.1	100				
10	1.6	100				

Table S12. Full-width at half-maximum (FWHM) and relative integration of the signal in the ^{19}F NMR spectra of $[S_{112}][FSI]$ at various temperatures above and below $T_{s\text{-}s}$ (presented in Fig 5 in the manuscript).

Temperature / °C	FWHM / kHz	Integration / %
-50	5.1	100
-40	3.6	100
-30	2.6	100
-10	1.5	100
0	1.2	100
10	1.0	100

Table S13. Full-width at half-maximum (FWHM) and relative integration of the components within the NMR signal in the ^{1}H NMR spectra of $[S_{(5)1}][FSI]$ at various temperatures above and below $T_{s\text{-}s}$ (presented in Fig 5 in the manuscript). An example of the deconvoluted spectra is shown in **Figure S14**.

	Component 1		Component 2		Component 3	
Temperature / °C	FWHM / kHz	Integration / %	FWHM / kHz	Integration / %	FWHM / kHz	Integration / %
-40	79.4	77.86	15.8	22.11	0.5	0.03
-30	73.0	79.0	16.0	20.9	1.3	0.1
-20	71.9	79.9	14.9	20.0	0.9	0.1
-10	7.4	100				
0	7.3	100				
10	7.2	100				

Table S14. Full-width at half-maximum (FWHM) and relative integration of the signal in the ^{19}F NMR spectra of $[S_{(5)1}][FSI]$ at various temperatures above and below $T_{s\text{-}s}$ (presented in Fig 5 in the manuscript).

Temperature / °C	FWHM / kHz	Integration / %
-40	50.4	100
-30	50.9	100
-20	50.9	100
-10	5.7	100
0	5.3	100
10	5.2	100

Table S15. Full-width at half-maximum (FWHM) and relative integration of the components within the NMR signal in the ^{1}H NMR spectra of $[S_{(5)2}][FSI]$ at various temperatures above and below $T_{s\text{-}s}$ (presented in Fig 5 in the manuscript). An example of the deconvoluted spectra is shown in **Figure S15**.

	Component 1		Component 2		Component 3	
Temperature / °C	FWHM / kHz	Integration / %	FWHM / kHz	Integration / %	FWHM / kHz	Integration / %
-30	59.9	95.7	8.5	2.4	1.6	1.9
-20	57.4	91.8	11.2	5.1	1.4	3.1
-10	55.1	83.0	12.4	10.0	1.2	7.0

10	1.0	100				
20	1.0	100				
30	1.0	100				

Table S16. Full-width at half-maximum (FWHM) and relative integration of the components within the NMR signal in the ^{19}F NMR spectra of $[S_{(5)2}][FSI]$ at various temperatures above and below $T_{s\text{-}s}$ (presented in Fig 5 in the manuscript).

	Component 1		**Component 2**	
Temperature / °C	**FWHM / kHz**	**Integration / %**	**FWHM / kHz**	**Integration / %**
-30	57.2	100		
-20	55.1	100		
-10	43.8	99.0	1.1	1.0
10	1.1	100		
20	1.1	100		
30	1.0	100		

Table S17. Full-width at half-maximum (FWHM) and relative integration of the components within the NMR signal in the 1H NMR spectra of $[N_{1111O1}][FSI]$ at various temperatures above and below $T_{s\text{-}s}$ (presented in Fig 5 in the manuscript).

	Component 1		**Component 2**	
Temperature / °C	**FWHM / kHz**	**Integration / %**	**FWHM / kHz**	**Integration / %**
-35	12.7	50.0	37.9	50.0
-25	12.6	54.9	36.5	45.1
-15	12.5	57.6	35.8	42.4
5	1.5	100		
15	1.0	100		
25	0.7	100		

Table S18. Full-width at half-maximum (FWHM) and relative integration of the signal in the ^{19}F NMR spectra of $[N_{1111O1}][FSI]$ at various temperatures above and below $T_{s\text{-}s}$ (presented in Fig 5 in the manuscript).

Temperature / °C	**FWHM / kHz**	**Integration / %**
-35	55.3	100
-25	53.1	100
-15	52.3	100
5	1.2	100
15	1.0	100
25	0.8	100

Pulsed-field gradient NMR

The diffusion coefficients of the cations and anions were determined by ^{1}H and ^{19}F pulsed-field gradient stimulated echo NMR (PFG-NMR). The samples were packed into a 4 mm magic angle spinning (MAS) rotor in an argon glovebox. Experiments were performed on a 7 T Bruker Avance III spectrometer equipped with a diff50 probe. Spectra were analysed using TopSpin software. Fast T_2 relaxation and slow diffusion in neat OIPCs can lead to weak signals in PFG-NMR, especially at low temperatures. Where possible, spectra were collected at multiple temperatures.

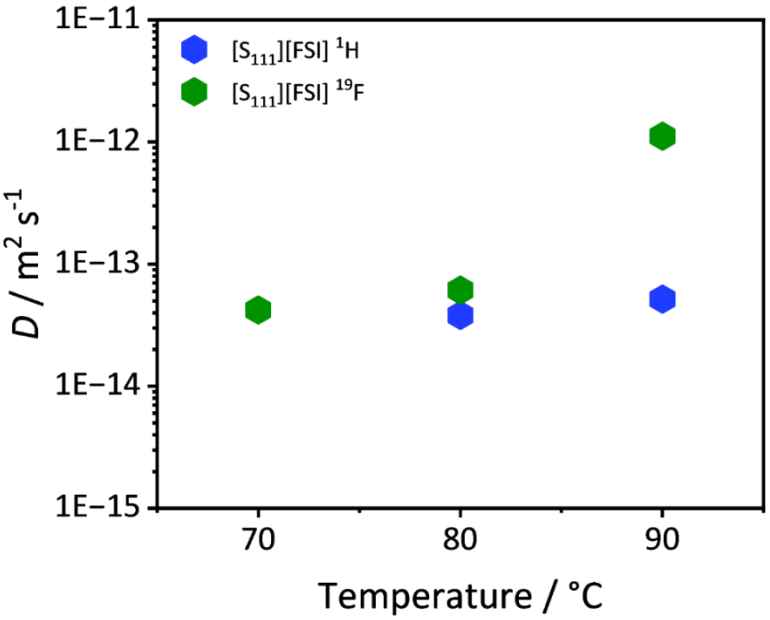

Figure S18. Diffusion coefficients of ^{1}H (blue) and ^{19}F (green) of $[S_{111}][FSI]$ at various temperatures, corresponding to cation and anion diffusion respectively.

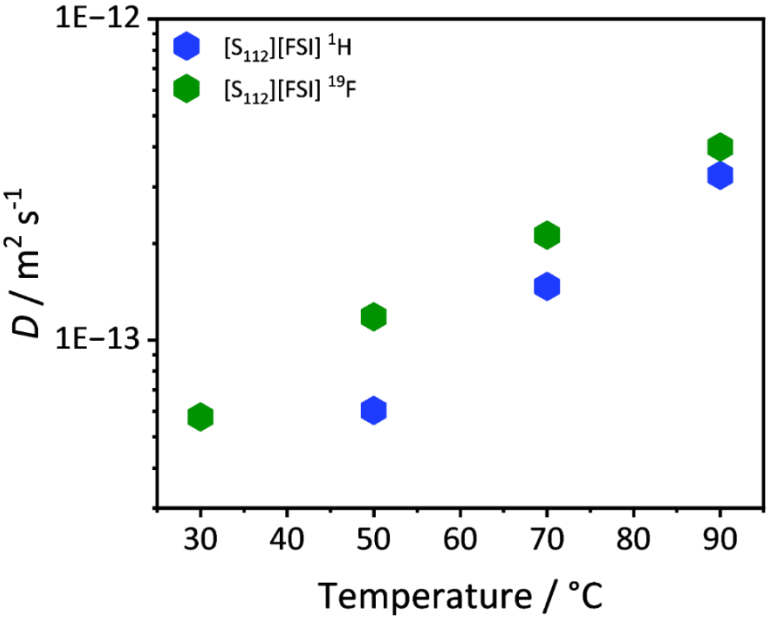

Figure S19. Diffusion coefficients of ^{1}H (blue) and ^{19}F (green) of $[S_{112}][FSI]$ at various temperatures, corresponding to cation and anion diffusion respectively.

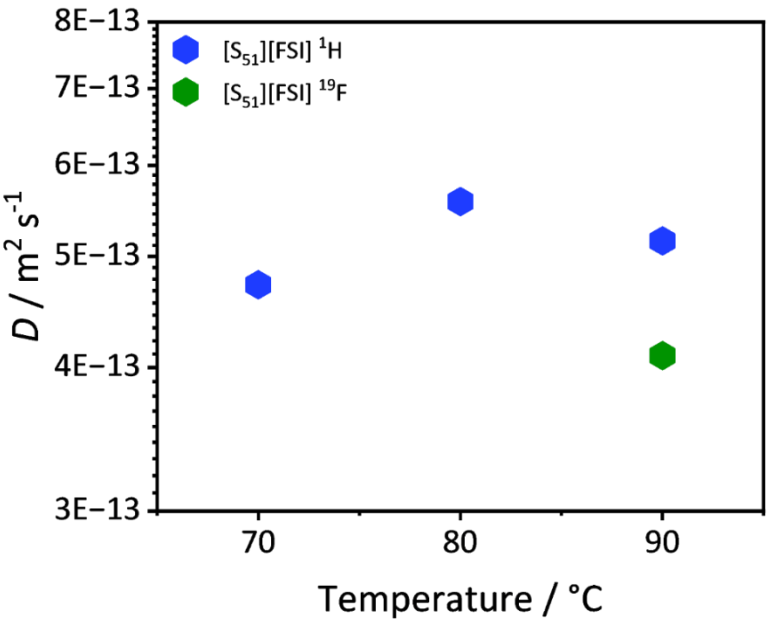

Figure S20. Diffusion coefficients of ^{1}H (blue) and ^{19}F (green) of $[S_{(5)1}][FSI]$ at various temperatures, corresponding to cation and anion diffusion respectively.

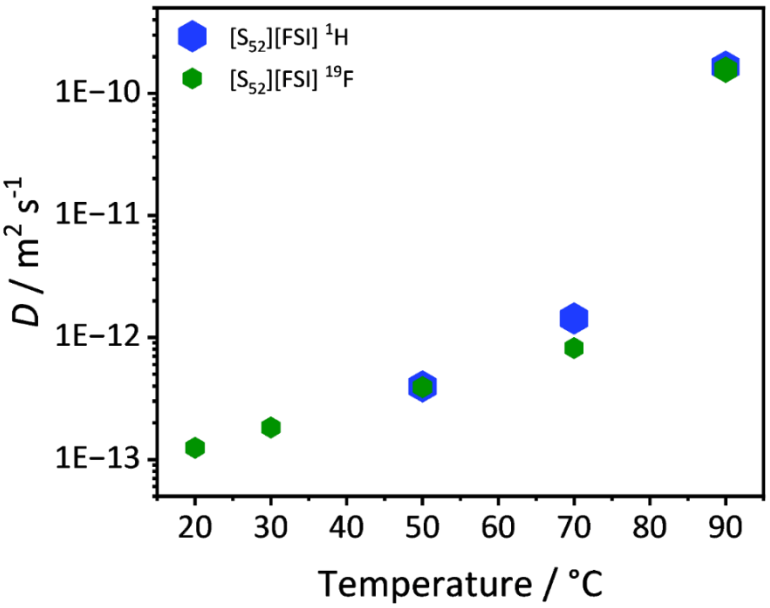

Figure S21. Diffusion coefficients of ^{1}H (blue) and ^{19}F (green) of $[S_{(5)2}][FSI]$ at various temperatures, corresponding to cation and anion diffusion respectively.

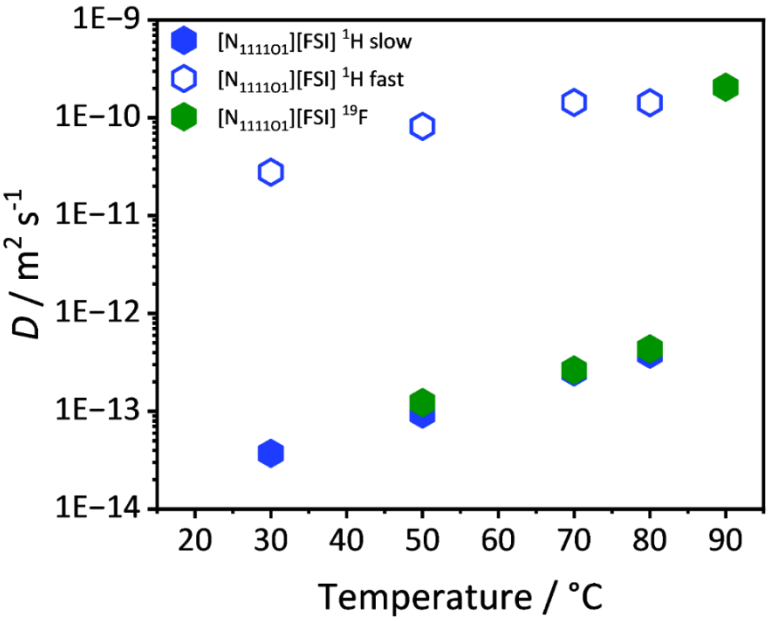

Figure S22. Diffusion coefficients of ^{1}H (blue) and ^{19}F (green) of [N_{1111O1}][FSI] at various temperatures, corresponding to cation and anion diffusion respectively.

1.5 Positron Annihilation Lifetime Spectroscopy (PALS)

The average pore size and relative quantity were analysed using positron annihilation lifetime spectroscopy (PALS). Measurements were performed with EG&G Ortec spectrometers operating in coincidence mode. Each of the samples consisted of two disk specimens of minimum 1 mm thickness, with each disk placed either side of a 1.85 MBq ^{22}NaCl positron point source, encapsulated in a Mylar envelope. Data acquisition involved a minimum of five spectra, each comprising 1×10^6 integrated counts. Data was collected on phase I of all of the OIPCs at room temperature, and in phase II for [S_{111}][FSI] and [N_{1111O1}][FSI] at -10 °C and -18 °C respectively. The sample holder was chilled using a wand chiller, and in both cases the cell was held at a temperature > 20 °C below its $T_{s\text{-}s}$ for at least two hours to ensure the phase I→II crystallisation transition had occurred prior to the commencement of data collection.

Spectral analysis was conducted using LTv9 software,[4] where the data were fitted to three lifetime components. The first component, fixed at 125 ps, corresponded to the annihilation of *para*-positronium (*p*-Ps), a bound state of a positron and an electron with opposite spin. The second component, approximately 400 ps, was associated with the direct annihilation of positrons with free electrons in the sample. The third and longest lifetime component represented the annihilation of *ortho*-positronium (*o*-Ps), a bound state of a positron and an electron with the same spin. The *o*-Ps lifetime (τ_3) was used to calculate the average free volume radius (*r*) via the Tao–Eldrup equation,[5,6] and the relative intensity I_3, was correlated to the average number of pores in the sample.

We collected PALS data on [N_{1111O1}][FSI] in phase I (at room temperature), which was consistent with the phase I PALS data we have reported for this salt previously (**Table S19**).

Table S19. A comparison of the PALS data reported for phase I of $[N_{1111O1}][FSI]$[7] and the equivalent room temperature data recollected in this work.

$[N_{1111O1}][FSI]$	Lifetimes, τ_3 / ns	Intensities, I_3 / %	Vacancy diameter / nm	Vacancy volume V_d / Å^3	FFV (PALS) / a.u.
Ref [7]	2.427 ± 0.020	11.2 ± 0.1	0.643 ± 0.003	139	1560 ± 21
This work	2.435 ± 0.024	10.9 ± 0.1	0.645 ± 0.004	141	1527 ± 45

2. Thermal and barocaloric properties

2.1 Construction of entropy curves

Isobaric entropy curves

To obtain the isobaric entropy curves, 1 bar heat flow data on heating (collected by DSC using a scan rate of 1 °C) was integrated, after baseline subtraction, between a temperature interval T_1 and T_2 (which are above and below $T_{s\text{-}s}$ respectively):

Equation 1

$$\Delta S_{ib} = \int_{T_1}^{T_2} \frac{1}{T} \frac{Q\ (P,T)}{T'}\ dT$$

Where T' is the ramping rate.

The heat capacity contribution, $S_c(T)$, was calculated from Equation 2 and added to the ΔS_{ib} curves calculated from Equation 1.

Equation 2

$$S_c(T) = \int_{T_1}^{T_2} \frac{C_p}{T}\ dT$$

The heat capacity of the low temperature phase was integrated from T_1 to the centre of the (approximately symmetrical) heat flow peak, after which the heat capacity of the high temperature phase was substituted into Equation 1. T_1 is set to a common starting point value for all entropy curves for a given OIPC. Heat capacity equations were obtained as linear fits of the regions above and below the solid-solid phase transition in calibrated heat capacity DSC experiments as shown in **Figure S11**.

Due to the use of DTA over DSC, to construct the ΔS_{ib} curves for various pressures, we used the heat flow data from the 1 bar DSC experiments and shifted it according to $dT_{s\text{-}s}/dp$, before re-integrating the data per Equation 1. For the exothermic transitions, we inverted the 1 bar heat flow data and shifted it according to both $dT_{s\text{-}s}/dp$ and ΔT_{hys} (with ΔT_{hys} defined as the lowest value observed in DTA experiments for each compound, as discussed in the manuscript). This may reduce the calculated barocaloric performance as endothermic transitions typically have much narrower peak widths compared to exotherms, however is valid as long as there is no reduction in enthalpy with increasing pressure, which we confirmed in previous work.[2]

Isothermal entropy curve construction

Pressure-induced entropy changes (from 1 bar to the applied pressure, p) were calculated from Equation 3:

Equation 3

$$\Delta S_{it}(1 \rightarrow p_1) = \Delta S_{ib}(p) - \Delta S_{ib}(1\ bar)$$

Maximum values of ΔS_{it} calculated for various pressure changes for each of the OIPCs, as shown in Fig 4A in the manuscript, are provided in **Table S20** -**Table S24**.

Adiabatic temperature changes

The maximum adiabatic temperature change that can be generated in the material for a given pressure change during the phase change, under adiabatic conditions, was calculated by transforming the $S_{ib}(T,p)$ data into $T(S,p)$ and then calculating the temperature difference, ΔT_{ad}, that would be generated for a pressure change under adiabatic (constant S) conditions:

$$\Delta T_{ad,comp}(1\ bar \rightarrow p) = T(S,p)_{cooling} - T(S,1\ bar)_{cooling}$$

for compression and

$$\Delta T_{ad,decomp}(p \rightarrow 1\ bar) = T(S,1\ bar)_{heating} - T(S,p)_{heating}$$

for decompression.

These are plotted as a function of starting temperature for compression and finishing temperature for decompression. Maximum values of ΔT_{ad} calculated on decompression and compression (as shown in Fig 4F in the manuscript) for various applied pressure changes are provided in **Table S20** -**Table S24**.

Refrigeration capacity and barocaloric strength

The refrigeration capacity (RC) for a given pressure change is calculated from:

$$RC = \Delta S_{\mathrm{it,rev,max}} \times \Delta T_{\mathrm{FWHM}}$$

Where ΔT_{FWHM} is the full-width at half maximum of the $\Delta S_{it,rev}$ curve (shaded regions in Fig 4B).

As this metric does not account for the work required to drive the cycle, RC can be normalised by the applied pressure change to calculate "barocaloric strength", i.e. RC/Δp. This allows direct comparison with other BC materials from the literature. The results from these calculations for various applied pressure changes, as shown in Fig 4E in the manuscript, are provided in **Table S20** -**Table S24**. A comparison of these values with some example leading BC materials from the literature are provided in **Table S25**.

Table S20. BC performance metrics for [S_{111}][FSI] calculated for a range of applied pressure changes (raw data for Fig 5 in the manuscript).

Pressure change / bar	100	200	300	500	600	800	1000
$\Delta S_{it,rev,max}$ / J kg^{-1} K^{-1}	9	64	130	256	304	305	305
FWHM / °C	0.2	0.7	1.4	2.9	3.8	6.7	9.5
RC / J kg^{-1}	2	47	183	737	1158	2033	2911
RC/Δp / J kg^{-1} bar^{-1}	0.0	0.2	0.6	1.5	1.9	2.5	2.9
$\Delta T_{ad,comp}$ / °C		2.8	4.2	6.9	8.4	11.1	13.9
$\Delta T_{ad,decomp}$ / °C		-2.8	-4.2	-6.9	-8.3	-11.1	-13.9

Table S21. BC performance metrics for [S_{112}][FSI] calculated for a range of applied pressure changes (raw data for Fig 5 in the manuscript).

Pressure change / bar	500	600	700	800	1000
$\Delta S_{it,rev,max}$ / J kg^{-1} K^{-1}	118	209	297	356	382
FWHM / °C	0.7	1.3	1.8	2.5	4.6
RC / J kg^{-1}	83	272	535	890	1757
RC/Δp / J kg^{-1} bar^{-1}	0.2	0.5	0.8	1.1	1.8
$\Delta T_{ad,comp}$ / °C	5.4	6.5	7.5	8.6	10.8
$\Delta T_{ad,decomp}$ / °C	-5.4	-6.5	-7.5	-8.6	-10.8

Table S22. BC performance metrics for [$S_{(5)1}$][FSI] calculated for a range of applied pressure changes (raw data for Fig 5 in the manuscript).

Pressure change / bar	600	800	1000
$\Delta S_{it,rev,max}$ / J kg^{-1} K^{-1}	157	266	304
FWHM / °C	1.1	2.1	3.7
RC / J kg^{-1}	171	549	1138
RC/Δp / J kg^{-1} bar^{-1}	0.3	0.7	1.1
$\Delta T_{ad,comp}$ / °C	5.6	7.4	9.3
$\Delta T_{ad,decomp}$ / °C	-5.6	-7.4	-9.3

Table S23. BC performance metrics for [$S_{(5)2}$][FSI] calculated for a range of applied pressure changes (raw data for Fig 5 in the manuscript).

Pressure change / bar	2200	2500	3000
$\Delta S_{it,rev,max}$ / J kg^{-1} K^{-1}	226	340	3340
FWHM / °C	1.6	4.5	10.7
RC / J kg^{-1}	368	1530	3638
RC/Δp / J kg^{-1} bar^{-1}	0.22	0.6	1.2
$\Delta T_{ad,comp}$ / °C	26.5	30.1	36.1
$\Delta T_{ad,decomp}$ / °C	-26.4	-30.0	-36.0

Table S24. BC performance metrics for $[N_{1111O1}][FSI]$ calculated for a range of applied pressure changes (raw data for Fig 5 in the manuscript).

Pressure change / bar	**600**	**800**	**1000**	**1200**
$\Delta S_{it,rev,max}$ / J kg^{-1} K^{-1}	15	141	267	271
FWHM / °C	0.4	1.4	3.2	6.1
RC / J kg^{-1}	6	193	846	1654
RC/Δp / J kg^{-1} bar^{-1}	0.0	0.2	0.8	1.4
$\Delta T_{ad,comp}$ / °C	8.5	11.3	14.1	16.9
$\Delta T_{ad,decomp}$ / °C	-9.4	-12.2	-15.0	-17.8

Table S25. Barocaloric effects and performance metrics for select barocaloric materials from the literature, alongside those reported here.

Material	$T_{s\text{-}s}$ (°C)	$dT_{s\text{-}s}/dp$ (K kbar^{-1})	$\Delta S_{s\text{-}s}$ (J kg^{-1} K^{-1})	ΔT_{hys} (°C)	p_{rev} (bar)	$\Delta S_{it,rev}$		*RC*		RC_{rev} / Δp (J kg^{-1} bar^{-1})	*Ref*
						J kg^{-1} K^{-1}	*p* (bar)	J kg^{-1}	*p* (bar)		
$[S_{111}][FSI]$	4	14.3	296	0.9	63	304	600	2910	1000	2.91	This work
$[S_{112}][FSI]$	-20	10.9	375	2.4	220	382	1000	1757	1000	1.76	This work
$[S_{(5)1}][FSI]$	-19	9.5	331	1.9	200	305	1000	1140	1000	1.14	This work
$[S_{(5)2}][FSI]$	-5	12.3	343	22.6	1837	340	2500	1530	2500	0.61	This work
$[N_{1111O1}][FSI]$	-9	14.5	258	8.9	614	267	1000	850	1000	0.85	This work
$[C_{i3}mpyr][TFSI]$	-37	12.1^{h}	91	0.5	42	92	350	0.86	1000	0.86	[2]
$[C_{i3}mpyr][FSI]$	-27	13.8^{h}	191	6	403	170	900	0.89	1000	0.89	[2]
$[N_{2222}][TFSI]$	4	23.7^{h}	160	8	342	154	600	2.0	1000	1.99	[2]
$[C_2mmor][FSI]$	11	12.1^{h}	240	5.3	521	240	1239	6.0	1000	0.60	[2]
$Fe[HB(tz)_3]_2$	59	21.4^{c}	99	0.2	10	89	150	179	150	1.19	[8]
$Fe_3(bntrz)_6(tcnset)_6$	45	25^{c}	80	2	80	80	300	564	300	1.88	[9]
$(NH_4)_2SO_4$	-51	-5.7^{h}	65	1	175	60	1000	276	1000	0.28	[10]
$[TPrA][Mn(dca)_3]$	57	23.1^{avg}	43	0.9	39	31	70	54	70	0.77	[11]
Neopentyl glycol	41	9.3^{c}	389	14	1505	450	2000	2800	2500	1.12	[12,13]
Ortho-carboborane	4	33^{h}	79	8	242	89	300	-	-	-	[14]
$(C_6H_{13})_2NH_2Cl$	6	28.1^{c}	203	2.2	78	71	150	-	-	-	[15]
NH_4I	-5	79	71	25	316	71	400	710	400	1.78	[16]
cyano-RbMnFeCo	-23	110	166	52	9.1	-	-	3700	900	4.1	[17]

* The superscript on values of $dT_{s\text{-}s}/dp$ indicate whether the value represents the shift of $T_{s\text{-}s}$ on heating (subscript *h*), cooling (subscript *c*) or the average between heating and cooling (*avg*). A negative value indicates a reverse barocaloric effect. ΔT_{hys} refers to the lowest observed value, e.g. $T_{s\text{-}s}$ onsets where available. As values of $\Delta S_{it,rev}$ and *RC* are dependent on pressure, these columns are split to indicate the pressure used to calculate the given value of *RC*. The $RC/\Delta p$ column uses the values of *RC* and the pressure value reported in the preceding column.

References

1 Q. Zhang, S. Liu, Z. Li, J. Li, Z. Chen, R. Wang, L. Lu and Y. Deng, *Chem. Euro. J.*, 2009, **15**, 765–778.

2 S. L. Piper, L. Melag, M. Kar, X. Xiao, E. F. May, K.-F. Aguey-Zinsou, D. R. MacFarlane and J. M. Pringle, *Science*, 2025, **387**, 56–62.

3 L. Jin, K. M. Nairn, C. M. Forsyth, A. J. Seeber, D. R. MacFarlane, P. C. Howlett, M. Forsyth and J. M. Pringle, *J. Am. Chem. Soc.*, 2012, **134**, 9688–9697.

4 J. Kansy, *Nucl. Instrum. Methods Phys. Res.*, 1996, **374**, 235–244.

5 M. Eldrup,D. Lightbody and J. N. Sherwood, *Chem. Phys.* 1981, **63**, 51–58.

6 S. Tao, *J. Chem. Phys.*, 1972, **56**, 5499–5510.

7 A. Warrington, C. S. M. Kang, C. Forsyth, C. M. Doherty, D. Acharya, L. A. O'Dell, N. Sirigiri, J. W. Boyle, O. E. Hutt, M. Forsyth and J. M. Pringle, *Mater. Chem. Front.*, 2022, **6**, 1437–1455.

8 J. Seo, J. D. Braun, V. M. Dev and J. A. Mason, *J. Am. Chem. Soc.*, 2022, **144**, 6493–6503.

9 M.Romanini, Y. Wang, K. Gürpinar, G. Ornelas, P. Lloveras, Y. Zhang, W. Zheng, M.Barrio, A. Aznar and A. Gràcia-Condal, B. Emre, O. Atakol, C. Popescu, H.Zhang, Y. Long, L. Balicas, J.-L. Tamarit, A. Planes, M. Shatruk and L. Mañosa, *Adv. Mater.*, 2021, **33**, 2008076.

10 P. Lloveras, E. Stern-Taulats, M. Barrio, J.-L. Tamarit, S. Crossley, W. Li, V. Pomjakushin, A. Planes, L. Mañosa and N. Mathur, *Nat. Commun.*, 2015, **6**, 8801.

11 J. M. Bermúdez-García, M. Sánchez-Andújar, S. Castro-García, J. López-Beceiro, R. Artiaga and M. A. Señarís-Rodríguez, *Nat. Commun.*, 2017, **8**, 15715.

12 B. Li, Y. Kawakita, S. Ohira-Kawamura, T. Sugahara, H. Wang, J. Wang, Y. Chen, S. I. Kawaguchi, S. Kawaguchi and K. Ohara, K. Li, D. Yu, R. Mole, T. Hattori, T. Kikuchi, S. Yano, Z. Zhang, Z. Zhang, W. Ren, S. Lin, O. Sakata, K. Nakajima and Z. Zhang, *Nature*, 2019, **567**, 506–510.

13 P. Lloveras, A. Aznar, M. Barrio, P. Negrier, C. Popescu, A. Planes, L. Mañosa, E. Stern-Taulats, A. Avramenko and N. D. Mathur, *Nat. Commun.*, 2019, **10**, 1803.

14 K. Zhang, R. Song, J. Qi, Z. Zhang, Z. Zhang, C. Yu, K. Li, Z. Zhang and B. Li, *Adv. Funct. Mater.*, 2022, **32**, 2112622.

15 J. Seo, R. Ukani, J. Zheng, J. D. Braun, S. Wang, F. E. Chen, H. K. Kim, S. Zhang, C. Thai and R. D. McGillicuddy, *J. Am. Chem. Soc.*, 2024, **146**, 2736–2747.

16 Q. Ren, J. Qi, D. Yu, Z. Zhang, R. Song, W. Song, B. Yuan, T. Wang, W. Ren and Z. Zhang, *Nat. Commun.*, 2022, **13**, 2293.

17 S. Ohkoshi, K. Nakagawa, M. Yoshikiyo, A. Namai, K. Imoto, Y. Nagane, F. Jia, O. Stefanczyk, H. Tokoro and J. Wang, *Nat. Commun.*, 2023, **14**, 8466.